

Convectively coupled equatorial waves within the MJO during CINDY/DYNAMO: slow Kelvin waves as building blocks

Kazuyoshi Kikuchi¹  · George N. Kiladis² · Juliana Dias² · Tomoe Nasuno³

Received: 27 October 2016 / Accepted: 18 August 2017 / Published online: 29 August 2017
© Springer-Verlag GmbH Germany 2017

Abstract This study examines the relationship between the MJO and convectively coupled equatorial waves (CCEWs) during the CINDY2011/DYNAMO field campaign using satellite-borne infrared radiation data, in order to better understand the interaction between convection and the large-scale circulation. The spatio-temporal wavelet transform (STWT) enables us to document the convective signals within the MJO envelope in terms of CCEWs in great detail, through localization of space–time spectra at any given location and time. Three MJO events that occurred in October, November, and December 2011 are examined. It is, in general, difficult to find universal relationships between the MJO and CCEWs, implying that MJOs are diverse in terms of the types of disturbances that make up its convective envelope. However, it is found in all MJO events that the major convective body of the MJO is made up mainly by slow convectively coupled Kelvin waves. These Kelvin waves have relatively fast phase speeds of 10–13 m s⁻¹ outside of, and slow phase speeds of ~8–9 m s⁻¹ within the MJO. Sometimes even slower eastward propagating signals with 3–5 m s⁻¹ phase speed show up within the MJO, which, as well as the slow Kelvin waves, appear to comprise major building blocks of the MJO. It is also suggested that these eastward propagating waves often occur coincident with

$n = 1$ WIG waves, which is consistent with the schematic model from Nakazawa in 1988. Some practical aspects that facilitate use of the STWT are also elaborated upon and discussed.

1 Introduction

The Madden–Julian Oscillation (Madden and Julian 1971, 1972) is the predominant intraseasonal oscillation in the tropics and has a profound influence on a wide range of weather and climate phenomena (e.g., Lau and Waliser 2012; Zhang 2013). Despite extensive studies over the past several decades, our understanding of the dynamics and physics of the MJO remains incomplete (e.g., Majda and Stechmann 2012; Waliser 2012; Wang 2012) and our ability to simulate the MJO with fidelity even in state-of-the-art numerical models remains unsatisfactory (e.g., Hung et al. 2013; Kikuchi et al. 2017).

Of the key processes associated with the initiation and maintenance of the MJO, it seems obvious that the interplay between convection and the large-scale circulation must play a crucial role, although our knowledge of these interactions is perhaps the most uncertain of all. The MJO is usually viewed as a coupled system consisting of a rather ill-defined planetary-scale convective envelope and associated large-scale circulation that move eastward at an average phase speed of 5–6 m s⁻¹ in the Indo-Pacific region. On the other hand, individual convective elements within the MJO envelope occur on much smaller scales, many of which are highly organized mesoscale convective systems (MCSs; Nakazawa 1988; Mapes and Houze 1993; Chen et al. 1996). A substantial fraction of these MCSs tend to occur in association with synoptic-scale equatorially-trapped waves first identified theoretically by Matsuno

✉ Kazuyoshi Kikuchi
kazuyosh@hawaii.edu

¹ International Pacific Research Center, School of Ocean and Earth Science and Technology, University of Hawaii at Manoa, 1680 East West Road, Post Bldg. 401, Honolulu, HI 96822, USA

² Physical Sciences Division, NOAA Earth System Research Laboratory, Boulder, CO, USA

³ Japan Agency for Marine–Earth Science and Technology, Yokohama, Japan

(1966). These are frequently referred to as convectively coupled equatorial waves (CCEWs; e.g., Takayabu et al. 1996; Wheeler and Kiladis 1999; Kiladis et al. 2009; Dias et al. 2012).

It stands to reason that for a complete understanding of the MJO, particularly in terms of the interaction between convection and large-scale circulation, it is of critical importance to understand the relationship between the MJO and the organization of convection within its envelope. For example, previous studies have pointed out the existence of convectively coupled Kelvin waves (Nakazawa 1988; Dunkerton and Crum 1995; Masunaga et al. 2006; Roundy 2008) and westward inertio-gravity (WIG) waves within the MJO convective envelope (Takayabu 1994b; Chen et al. 1996; Takayabu et al. 1996; Haertel and Johnson 1998). Nevertheless, in contrast to these case studies, recent attempts to statistically identify a systematic relationship between the MJO and CCEWs have proven elusive. In particular, using a correlation approach between MJO activity and space–time spectral variance, Dias et al. (2013, 2017) found that there is no strong preferred scale of high frequency organization that is ubiquitous to the MJO.

The purpose of this study is to examine the relationship, from a morphological standpoint, between the MJO and CCEWs by exploiting data from the Cooperative Indian Ocean Experiment on Intraseasonal Variability in the Year 2011 (CINDY2011)/Dynamics of the MJO (DYNAMO) (Yoneyama et al. 2013). The CINDY/DYNAMO field experiment was designed to advance our understanding of the initiation process of the MJO in the Indian Ocean (IO). Fortunately, robust MJO events were observed during the observing period, providing an invaluable opportunity for studying various aspects of the MJO¹ including large-scale circulation, cloud populations, and air–sea interaction, among others. The use of the spatio-temporal wavelet transform (STWT) is advantageous for this work. The STWT is an extension of the classical wavelet transform (WT) and is able to describe the space–time scales of a space–time signal at a given location and time, enabling us to document the extent, or lack of, homogeneity and stationarity in a signal in great detail. Although the fundamental description of the STWT and initial results using the case study of Nakazawa (1988) were presented in Kikuchi and Wang (2010), some practical aspects of the STWT approach have not been rigorously addressed in the past. In addition to analyzing the CINDY/DYNAMO period in some detail, this study also considers issues such as the representation of the STWT spectra, sensitivity to STWT resolution, and their significance testing.

¹ A relatively comprehensive literature list can be found at <https://www.eol.ucar.edu/node/471/publications>.

2 Data

High resolution irradiance data has been proven to be extremely useful in the study of tropical convection that occurs in association with large-scale circulations (e.g., Nakazawa 1988; Takayabu 1994a; Wheeler and Kiladis 1999). For this study, we utilize a high-resolution brightness temperature (T_b) dataset using globally merged infrared T_b data (Janowiak et al. 2001). The original resolution of the data is 30 min in time and 4 km in horizontal space. For convenience, we constructed 3-h T_b data at 0.5° × 0.5° horizontal resolution for the period March 2000 through December 2013. The resolution of this dataset matches that of the Cloud Archive User Service (CLAUS) T_b data (Hodges et al. 2000), available for the period July 1983 through June 2009, that has been widely used to study CCEWs in many recent studies (e.g., Kiladis et al. 2009). We calibrated the merged infrared data to CLAUS by adjusting their means and variances to match at each grid point for the overlapping period. By applying a temporal linear interpolation, the dataset has no missing values within the tropics between 30°S–30°N. In this study we focus on the CINDY/DYNAMO observing period (October 2011–March 2012) for comparison with many other studies of that period (e.g., Gottschalck et al. 2013; Johnson and Ciesielski 2013; Yoneyama et al. 2013).

In calculating space–time spectra, we followed steps taken in previous studies (e.g., Wheeler and Kiladis 1999; Kikuchi 2014). First, we preprocess the data by removing the linear trend, and the first three harmonics of the climatological annual cycle. The data were then separated into symmetric and antisymmetric components about the equator. Spectra were calculated at each latitude and averaged over 15°S and 15°N and the spectral features are insensitive to the choice of latitudinal averaging (not shown). To minimize end effects, STWT spectra were calculated using the data from July 2011 through June 2012.

3 Spatio-temporal wavelet transform (STWT)

The STWT was documented by Kikuchi and Wang (2010), although we present more comprehensive and updated description of the method with additions or refinements including considerations of zonal wavenumber 0 component, statistical significance assessment, and energy conversion from STWT space to Fourier space (“Appendix”). The STWT was designed to accurately deal with spatial propagation information. The STWT W of a signal g as a function of space x and time t is defined as (e.g., Antoine et al. 2004)

$$\begin{aligned} W(b, \tau; a, c) &= \int_{-\infty}^{\infty} dx \int_{-\infty}^{\infty} dt g(x, t) \psi_{b, \tau; a, c}^*(x, t) \\ &= a \int_{-\infty}^{\infty} dk \int_{-\infty}^{\infty} d\omega \hat{g}(k, \omega) \hat{\psi}_{b, \tau; a, c}^*(k, \omega) e^{i(kb + \omega\tau)} \end{aligned} \quad (1)$$

where $\psi_{b,\tau,a,c}^*(x, t) = a^{-1}\psi^*((x - b)/ac^{1/2}, (t - \tau)/ac^{-1/2})$ is the mother wavelet with a scale parameter $a \in \mathbb{R}^+$, a speed tuning parameter $c \in \mathbb{R}^+$, and a translation (position in space and time) parameter $(b, \tau) \in \mathbb{R}^2$, with k representing zonal wavenumber and ω frequency, $*$ and \wedge denoting the complex conjugate and the Fourier transform (FT), respectively (see “Appendix” for the relationship between (a, c) and (k, ω)). It is evident that $\psi_{b,\tau,a,c}^*$ becomes singular as $c \rightarrow \infty$ as the STWT is intended to deal with translating signals. As for its application to tropical convection, however, we are also interested in the limit $c = \infty$ (i.e., zonal wavenumber $k = 0$).

For $c = \infty$, we exploit the one dimensional version of the WT

$$W(\tau; a, \infty) = \int_{-\infty}^{\infty} dt G(t) \psi_{\tau,a}^*(t) \tag{2}$$

$$= a^{1/2} \int_{-\infty}^{\infty} d\omega \hat{G}(\omega) \hat{\psi}^*(a\omega) e^{i\omega\tau}$$

where $\psi_{\tau,a}^*(x, t) = a^{-1/2}\psi^*((t - \tau)/a)$ and $G(t)$ is the zonal average of $g(x, t)$ at time t .

Energy conservation is written as

$$\frac{1}{C_{\psi_{c \neq \infty}}} \int_0^\infty \frac{da}{a^3} \int_0^\infty \frac{dc}{c} \int_{-\infty}^\infty db \int_{-\infty}^\infty d\tau |W(b, \tau, a, c)|^2$$

$$+ \frac{1}{C_{\psi_{c = \infty}}} \int_0^\infty \frac{da}{a^2} \int_{-\infty}^\infty d\tau |W(\tau, a, \infty)|^2$$

$$= \int_{-\infty}^\infty dx \int_{-\infty}^\infty dt |g(x, t)|^2 = \int_{-\infty}^\infty dk \int_{-\infty}^\infty d\omega |\hat{g}(k, \omega)|^2 \tag{3}$$

where

$$C_{\psi_{c \neq \infty}} = (2\pi)^2 \int_0^\infty \frac{dk}{k} \int_0^\infty \frac{d\omega}{\omega} |\hat{\psi}_{c \neq \infty}^*(k, \omega)|^2 < \infty \tag{4}$$

$$C_{\psi_{c = \infty}} = 2\pi \int_0^\infty \frac{d\omega}{\omega} |\hat{\psi}_{c = \infty}^*(\omega)|^2 < \infty \tag{5}$$

It turns out that the energy conservation holds to within more than 99% accuracy in the cases considered in this study.

The original signal can be reconstructed from W as follows:

$$f(x, t) = \frac{1}{C_{\delta_{c \neq \infty}}} \int_0^\infty \frac{da}{a^2} \int_0^\infty \frac{dc}{c} W(x, t; a, c)$$

$$+ \frac{1}{C_{\delta_{c = \infty}}} \int_{-\infty}^\infty \frac{da}{a^{1/2}} W(\tau; a, \infty) \tag{6}$$

where

$$C_{\delta_{c \neq \infty}} = 2\pi \int_0^\infty \frac{dk}{k} \int_0^\infty \frac{d\omega}{\omega} \hat{\psi}_{c \neq \infty}^*(k, \omega) < \infty \tag{7}$$

$$C_{\delta_{c = \infty}} = 2\pi \int_0^\infty \frac{d\omega}{\omega} \hat{\psi}_{c = \infty}^*(\omega) < \infty \tag{8}$$

As in energy, the above reconstruction formula holds numerically with excellent accuracy. Also the formula can be used to construct a STWT-based space–time filter. We have checked the consistency in filtered fields between the STWT-based and the Fourier-based (Wheeler and Kiladis 1999) space–time filters. To save computer resources, we use the Fourier-based filter in the discussion in Sect. 5

Because of the good correspondence between the wavelet scale and the Fourier scale (Meyers et al. 1993), it is reasonable to choose the Morlet function (a complex sinusoid within a Gaussian envelope) as the mother wavelet

$$\psi_{c \neq \infty}(x, t) = e^{i(k_0 x + \omega_0 t)} e^{-(x^2 + t^2)/2} \tag{9}$$

$$\psi_{c = \infty}(t) = e^{i\omega_0 t} e^{-t^2/2} \tag{10}$$

It is evident that k_0 and ω_0 determines the properties (i.e., trade-off between time resolution and frequency resolution) of the Morlet wavelet and $|k_0|, |\omega_0| \geq 5$ should be chosen to approximately satisfy the admissibility conditions [(4) and (5)] (see e.g., Kumar and FoufoulaGeorgiou 1997). Here we set $|k_0| = \omega_0 = 6$, which is a popular choice (e.g., Torrence and Compo 1998). Note that positive and negative k_0 correspond to eastward and westward moving patterns, respectively.

Figure 1a shows the space–time structure of the Morlet wavelet. It follows from Eq. (9) that the amplitude of the envelope decreases to e^{-1} at a distance of $\sqrt{2}$ in non-dimensional space and time (e-folding scale). Within the e-folding scale, about three wavelengths are contained. The heterogeneous treatment of space and time in the STWT enables it to handle phase propagation accurately. Figure 1b illustrates how the Morlet wavelets for different scales and speed tuning parameters are represented in Fourier space for the parameters $|k_0| = \omega_0 = 6$. It is evident that each wavelet is aligned in a way that the energy is concentrated along a constant phase speed, indicating sensitivity to the phase speed. Also evident is that the localization of energy is stronger at larger scales due to Heisenberg’s uncertainty principle (i.e., trade-off between time localization and frequency localization, e.g., Kumar and FoufoulaGeorgiou 1997; Addison 2002).

In practice, the wavelet scale and speed tuning parameter are discretized as $a_j = a_0 2^{j\delta_j}, c_q = c_0 2^{q\delta_q}, j = 1, 2, \dots, J$ and $q = 1, 2, \dots, Q$. The values of a_0, c_0, J , and Q must be chosen to resolve the smallest and largest space-time scales of interest. The performance of the STWT thus depends on the choices of δ_j and δ_q (scale and speed tuning parameter resolutions). For simplicity, we consider several homogenous cases where $\delta_j = \delta_q$ (Table 1). It is apparent that the magnitudes of J and Q are inversely proportional to the values of δ_j and δ_q . The choice of δ_j and

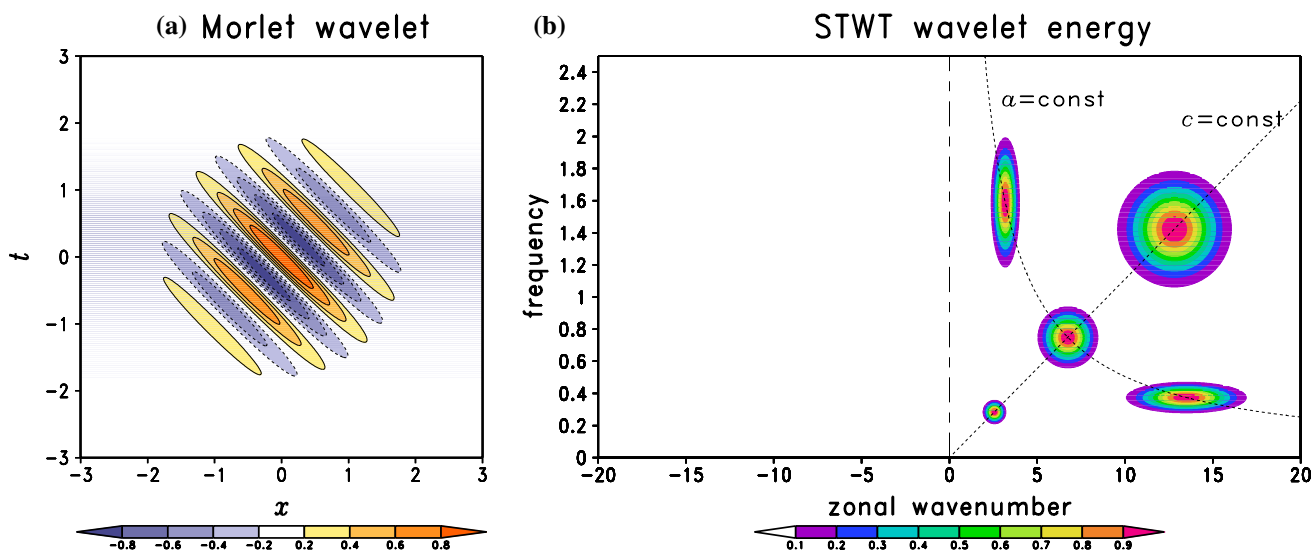


Fig. 1 Characteristics of the Morlet wavelet used in this study. **a** Space–time structure of the real part of the Morlet wavelet ($\psi(x, t) = e^{i(k_0x + \omega_0t)} e^{-(x^2 + t^2)/2}$) and **b** schematic showing how each

STWT wave component is represented in the Fourier space. *Shading* represents the amplitude of the normalized Morlet wavelet ($a\hat{\psi}_{a,c}^* = e^{-(ac^{1/2}k - k_0)^2/2} e^{-(ac^{-1/2}\omega - \omega_0)^2/2}$)

Table 1 Summary of computational costs

$\Delta j, \Delta q$	0.05	0.1	0.2	0.4	0.8	Fourier
Approximate number of points $[(2 \times Q + 1) \times J]$	110,000	30,000	7000	1000	600	1

The numerical values in the upper row represent the resolution of the STWT and those in the lower row represent the corresponding total numbers of points (i.e., number of FFTs) used to conduct STWT calculation

δ_q determines the trade-off between accuracy and computational costs.

The STWT spectrum is computed using Eqs. (1) and (2) by means of a fast FT (FFT). For each discretized a and c the FFT is calculated, and thus the computational costs for the STWT are roughly proportional to $(2 \times J + 1) \times Q$. For instance, at the lowest resolution ($\delta_j = \delta_q = 0.8$) about 600 times more computational costs are required than the FT and at the highest resolution the computational cost compared to the FT is increased by about 110,000 times!

Another important practical aspect concerns how to assess the statistical significance of spectral peaks. For a local STWT spectral peak, as in the FT, the degrees of freedom (DOF) is expected to be 2 for each scale (or bin). For an averaged STWT spectrum over space and time, in analogy with Torrence and Compo (1998), the effective DOF (EDOF) ν can be represented in the following form

$$\nu = 2 \sqrt{\left[1 + \left(\frac{n_t \delta t}{2\tau_e} \right)^2 \right] \left[1 + \left(\frac{n_x \delta x}{2b_e} \right)^2 \right]} \tag{11}$$

where $\tau_e = \sqrt{2ac}^{-1/2}$ and $b_e = \sqrt{2ac}^{1/2}$ are the e-folding time and space scales, respectively. This estimate can be

intuitively understood as follows: ν should be proportional to the number of wave packets in a period of time ($\sim n_t \delta t / 2\tau_e$) as well as to the number of wave packets in a length of space ($\sim n_x \delta x / 2b_e$). In the limit $n_t, n_x \rightarrow 1$ (i.e., no averaging), ν should be 2. Similarly, at $k = 0$ the EDOF is estimated as

$$\nu = 2 \sqrt{1 + \left(n_t \delta t / 2\tau_{e,k=0} \right)^2} \tag{12}$$

where the e-folding time scale $\tau_{e,k=0} = \sqrt{2a_{k=0}}$, and $a_{k=0} = 2\pi / 1.03\omega$. It turns out that this estimate is more conservative than that of Torrence and Compo (1998). The actual distribution of the EDOF for the case of CINDY/DYNAMO is discussed in the next section.

4 CINDY/DYNAMO overview

Figure 2 shows an overview of the convective episodes that took place during the CINDY/DYNAMO in terms of a Hovmöller diagram of Tb averaged over 7.5°S and 7.5°N. It is evident that convection tends to be clustered on intra-seasonal timescale over the warm pool region. Contours of MJO-filtered Tb anomalies are obtained by filtering for

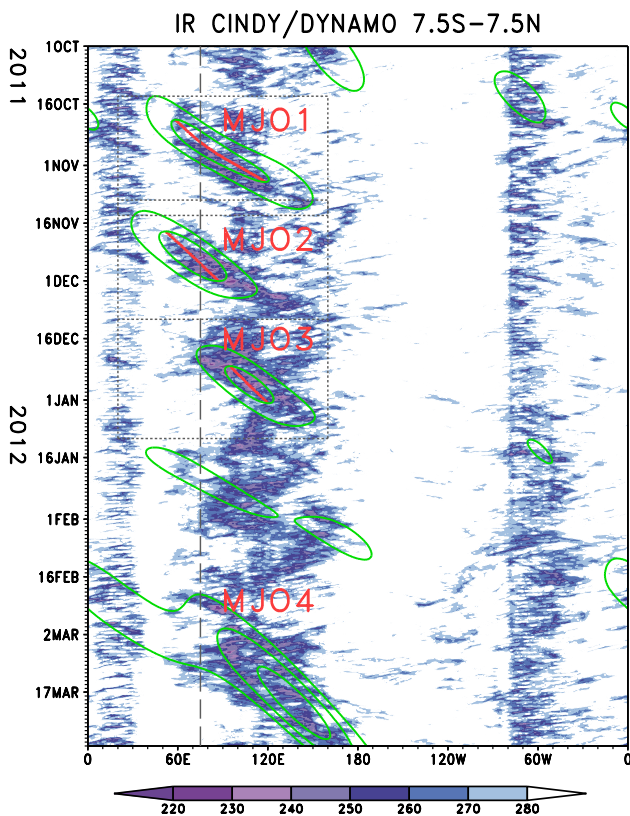


Fig. 2 Longitude-time section of T_b along the equator averaged over 7.5°S and 7.5°N during CINDY/DYNAMO period (October 2011–31 March 2012). Contours denote MJO-filtered (zonal wavenumbers 1–6 and frequencies $1/96$ – $1/25$ cpd) T_b anomalies with interval 4 K and only negative values are drawn. Regions denoted by dashed boxes are shown in greater detail in Figs. 6, 7 and 8. Red curves indicate MJO convective centers for the three major MJO events (see Sect. 5.3 for details). The dashed line is drawn along 75°E where the observing network was formed

eastward zonal wavenumbers 1 through 6 and 25–90 day periods using a FT. These contours suggest that there were four or five “MJO-like” events. Based on objective MJO indices including the all-season Real-time Multivariate MJO (RMM) index (Wheeler and Hendon 2004), the all-season OLR-based MJO index (OMI) (Kiladis et al. 2014), and the bimodal intraseasonal oscillation (Bi-ISO) index (Kikuchi et al. 2012), the events that were initiated over the IO in October, November, and February are viewed as relatively robust MJO events (labelled as MJO1, MJO2, and MJO4, respectively), with amplitudes in all indices exceeding 1 for at least a week.² The event that occurred in December (referred to here as MJO3 as in Yoneyama et al. (2013) and as a “mini-MJO” by Gottschalck et al. (2013)) is identified

² The time series of the RMM index can be found at <http://poama.bom.gov.au/project/maproom/RMM/>, OMI indices are at <http://www.esrl.noaa.gov/psd/mjo/mjindex/> and Bi-ISO index can be found at http://iprc.soest.hawaii.edu/users/kazuyosh/Bimodal_ISO.html.

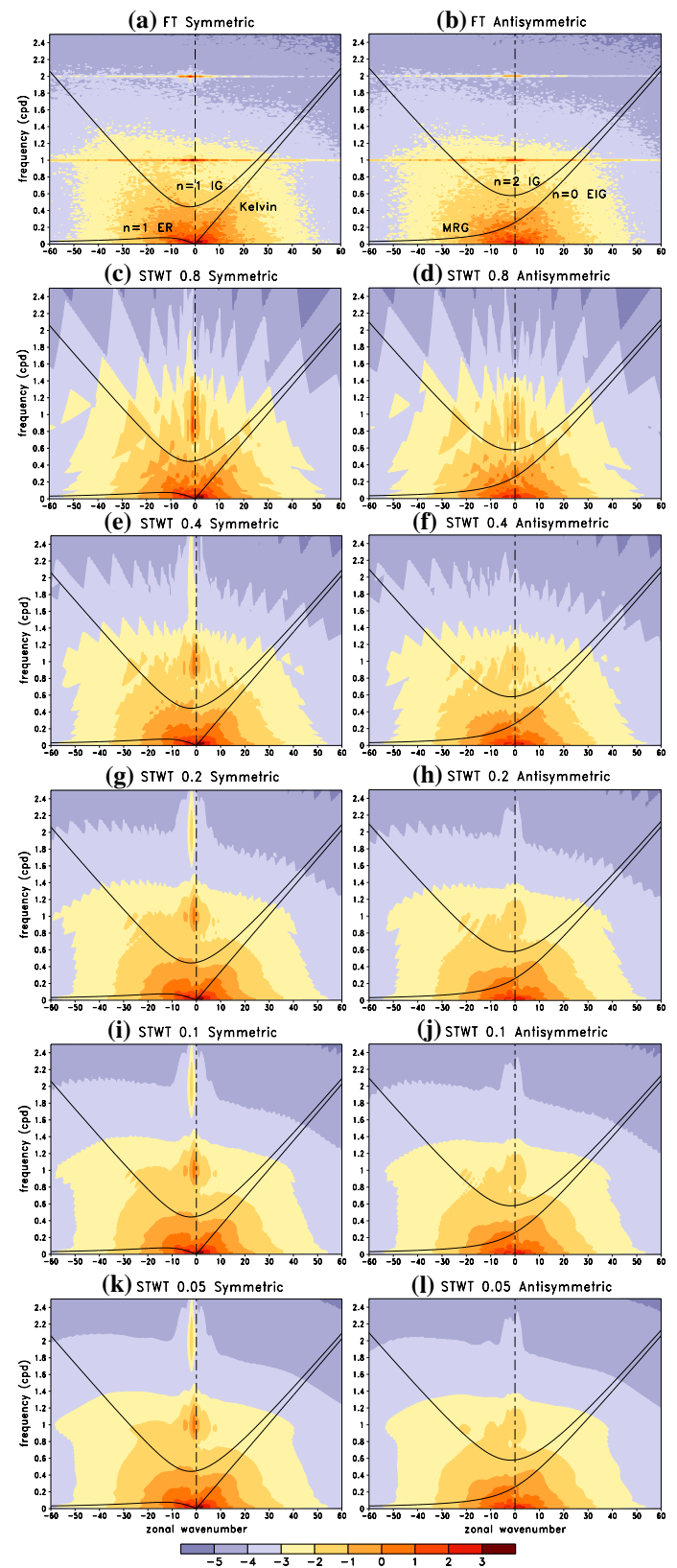
as a much weaker event by these criteria. The event that occurred in January was identified as a weak MJO by the OMI and Bi-ISO index, while not by the RMM index, and convection does not appear to be very organized over the central IO. It is implied, however, from Fig. 2 that the initiation of convection in MJO4 was rather ambiguous. In addition, many studies (e.g., Sobel et al. 2014; Johnson et al. 2015; Powell and Houze 2015b; Hannah et al. 2016) primarily focused on the MJO events that occurred in the intensive observing period (IOP), 1 October 2011–15 January 2012. Given these considerations, we focus on three MJO events (MJO1, MJO2, and MJO3) and analyze them in more detail throughout the following discussion.

Although it is not customary to identify spectral peaks from shorter periods of data, it is instructive to examine the CINDY/DYNAMO period to understand the nature of the STWT spectra in comparison to the conventional FT approach, and to place the convective events during this period in historical context through comparisons with spectra based on long-term data. Figure 3 shows the FT and several different resolution STWT spectral estimates in linear space–time wavenumber and frequency plots (see “Appendix” for details), over the entire global longitude range for the CINDY/DYNAMO period. The FT spectra were obtained in a conventional manner similar to the one developed by Wheeler and Kiladis (1999).

Overall the STWT spectra at different resolutions display a similar appearance to each other, while serrations due to insufficient sampling are evident at lower resolutions. These serrations are more evident at higher frequencies and/or larger wavenumbers due to the scale dependence of the STWT (Fig. 1b). At higher resolutions from 0.2 to 0.05 the detailed structures are very similar to each other, and serrations are barely detectable at the highest resolution. Based on this result, we conclude that using a resolution higher than 0.2 is optimal.

The STWT spectra and FT spectra yield consistent results, whereas the STWT spectra are smoothed due to the uncertainty principle, in particular at higher frequencies and larger wavenumbers. A casual inspection of either the STWT or FT spectra suggests the presence of spectral peaks that correspond to several types of CCEWs predicted theoretically by Matsuno (1966), such as Kelvin, equatorial Rossby (ER), $n = 1$ westward inertio-gravity (WIG), $n = 0$ eastward IG (EIG), and mixed Rossby-gravity (MRG) waves (Wheeler and Kiladis 1999). In addition, substantial power is concentrated in the MJO range (zonal wavenumbers of 1–5 and eastward frequencies of 0.03–0.01) in the symmetric component and at the diurnal and semidiurnal timescales in both the symmetric and antisymmetric components, which are much more apparent in the FT spectra. The absence of sharp spectral peaks in the STWT spectra is due to the smoothing nature of the method (Fig. 1b), leading to spectral

Fig. 3 Zonal wavenumber-frequency spectral estimates for the CINDY/DYNAMO period (October 2011–March, 2012) based on the FFT (*top*), and the STWT (*lower panels*) for the symmetric (*left*) and antisymmetric (*right*) components. The base-10 logarithm is taken. The STWT spectra are averaged spectra over the entire longitude and IOP period. The resolution ($\delta_j = \delta_q$) of the STWT spectra vary from 0.8 to 0.05. Dispersion curves for Kelvin, $n=1$ equatorial Rossby, $n=1$ and 2 inertio gravity, $n=0$ eastward inertio gravity and mixed Rossby gravity waves with equivalent depth of 25 m are shown by *solid curves* for reference



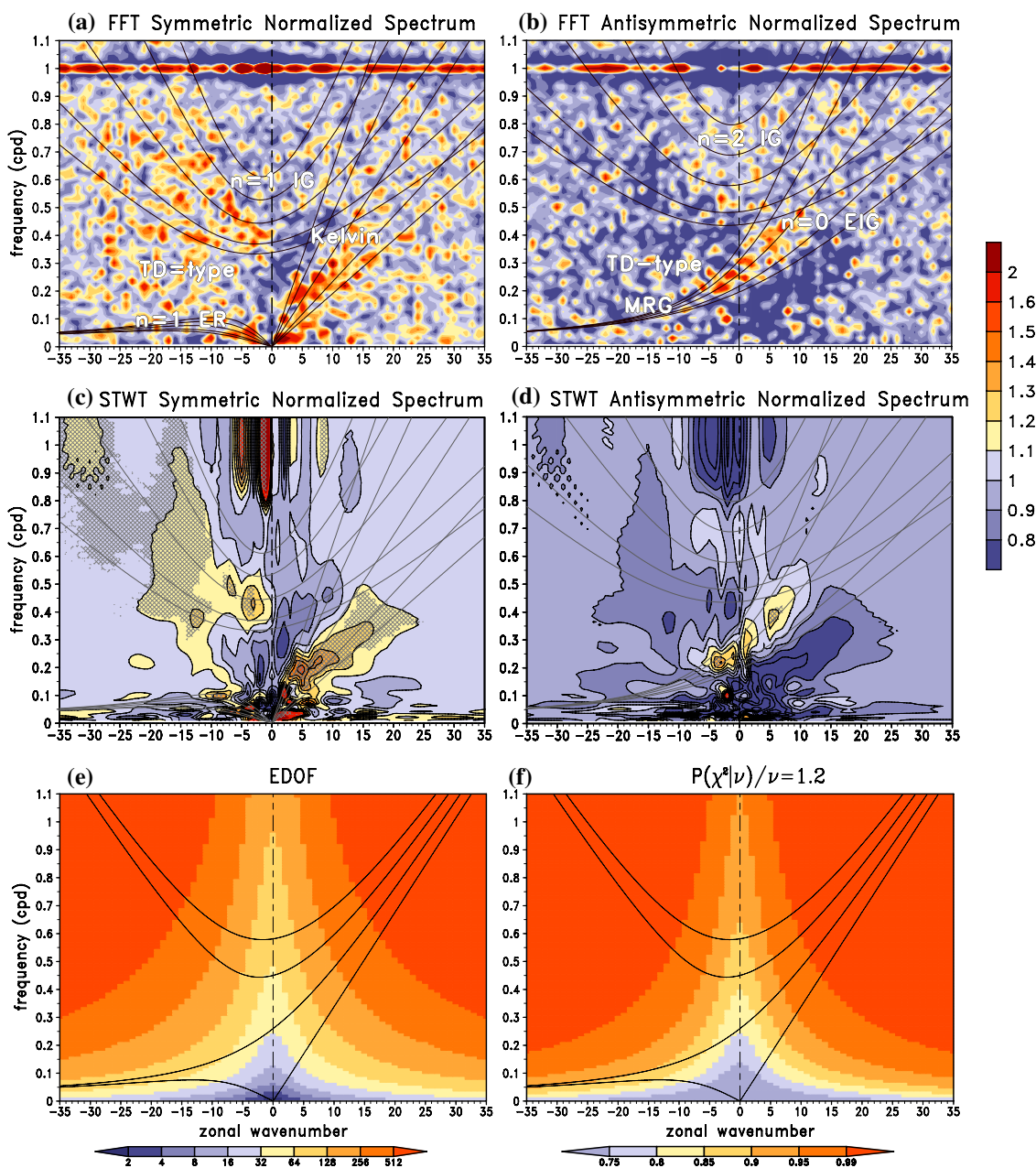


Fig. 4 Normalized zonal wavenumber-frequency spectra based on the (top) FFT, and (middle) the STWT for the symmetric (left) and antisymmetric (right) components in conjunction with, for the STWT spectra, **e** the effective degrees of freedom according to Eq. (11) and **f** the corresponding significance level at which normalized spectral peak of value 1.2 passes. The resolution in the calculation of the STWT spectra is 0.05. The background spectra used to normalize the

spectra was obtained by applying the same method as in Wheeler and Kiladis (1999) to the raw spectra shown in Fig. 3. As in Fig. 3, the STWT spectra are the average ones over space and time. Dispersion curves for various equatorial waves with equivalent depths of 8, 12, 25, 50, and 90 m are shown by solid curves. Cross hatches in **c** and **d** indicate where the spectral peak is statistically significant at the 90% level

peaks spread in frequency around the diurnal and semidiurnal cycles as opposed to peaks spread in wavenumber as in the FT spectra.

The prominence of CCEW peaks becomes more evident when the spectra are normalized by a background (Fig. 4). Although there is no consensus on the best approach to use

in estimating the background spectrum (Masunaga et al. 2006; Hendon and Wheeler 2008; Kikuchi 2014), for the sake of comparison, we estimated the background spectrum in the manner following Wheeler and Kiladis (1999) based on the raw data during the CINDY/DYNAMO period. The FT and STWT spectra yield quite consistent results,

although the FT spectra are much noisier. It is evident that several types of CCEWs were pronounced including the MJO, and Kelvin, $n=1$ WIG, ER, $n=0$ EIG, and MRG waves. The STWT spectra provide more coherent results at the expense of spectral resolution, which results in more smoothing when compared to the FT spectra. The FT spectra have ~ 4 ($\approx 2 \times 183/96$) EDOF at each scale (bin) based on the most conservative estimate (assuming each latitude is not independent from any others), whereas the averaged STWT spectra have more EDOF at most scales (Fig. 4e), as discussed in the previous section. In addition, Fig. 4f shows how the significance of a given ratio of a signal with respect to the background will vary with scale, unlike that in an FT spectrum where the EDOF is assumed to be constant for each bin. As a result, spectral peaks significant at the 90% level such as Kelvin, ER, WIG, and MRG-EIG waves are found in the STWT spectra, as shown by the crosses in Fig. 4c, d.

Despite the fact that only 183 days were used, the appearance of the STWT spectra in particular bear a strong resemblance to global FT spectra based on long-term data (e.g., Fig. 1 of Kiladis et al. 2009), with the exception of the lack of $n=2$ WIG waves in Fig. 4d during CINDY/DYNAMO. In both spectra, significant peaks corresponding to Kelvin, ER, $n=1$ WIG, and MRG/EIG exist with enhanced power concentrating in the range of the equivalent depth (h_e) 12–50 m. One notable difference from long-term spectra in the Kelvin wave peak concerns its apparent dispersion, as implied by a decrease of h_e with increasing wavenumber (k) and frequency (f). This is also often seen in localized FT spectra (Dias and Kiladis 2014). We address this issue further below. Also prominent are the diurnal peaks, which are primarily localized at wave -1 and -5 in the STWT in the symmetric component but more spread out across all wavenumbers in the FT spectra.

5 MJO and CCEWs relationship revealed by STWT

While the spectra discussed above were based on global data, an advantage of the STWT approach is that it can efficiently localize spectral signals in space and time. This section concerns the individual MJO events observed during the CINDY/DYNAMO period with a primary focus on the IO, in particular at 75°E , where the observational network in the field was centered (e.g., Yoneyama et al. 2013), and 100°E , at the eastern edge of the IO.

5.1 Average spectra

We first show in Fig. 5 the time-averaged local STWT spectra centered on 75°E and 100°E over the entire CINDY/

DYNAMO period, normalized by their local background spectra, respectively. The local background spectra were obtained in the same manner as the global background spectrum except the time-averaged (October 2011–March 2012) local spectrum centered at each longitude was used. Note that the overall structures of the spectra normalized by the global, instead of the local, background spectrum do not appear to be very different (not shown). In addition, the spectra normalized by the local background yield more conservative estimates of statistical significance, as this is a relatively convectively active longitude, so we advocate this approach over the use of a global background spectrum.

The overall features of the spectra at 75°E and 100°E are similar to the global spectra (Fig. 4c, d). As in the global spectra, certain types of CCEWs stand out that include Kelvin, $n=1$ WIG, ER, and MRG/EIG waves. As for the Kelvin waves, the energy is more concentrated at a smaller $h_e \sim 17$ m, which is consistent with the localized climatological FT spectra for the IO sector of Dias and Kiladis (2014). Again, we see that the Kelvin wave peaks are shifted toward smaller h_e at higher wavenumbers and frequencies. This dispersive behavior is stronger for Kelvin waves at 75°E than at 100°E . It should be also noted that the $n=1$ WIG waves contain a strong diurnal cycle peak at these locations. This peak is more pronounced at 100°E due to its proximity to the Maritime Continent where pronounced off-shore moving diurnal gravity waves tend to be generated to the west of Sumatra (e.g., Yang and Slingo 2001; Mori et al. 2004; Kikuchi and Wang 2008; Kubota et al. 2015).

5.2 Individual MJO events

To examine how CCEWs are associated with individual MJO events during CINDY/DYNAMO, Figs. 6, 7 and 8 show localized STWT spectra at 75°E and 100°E in conjunction with Hovmöller diagrams centered in time on the three MJO events identified above. From now on we focus on the symmetric component, because the antisymmetric component does not have very prominent spectral peaks, consistent with the relative lack of convectively coupled MRG/EIG activity over the IO as compared to the Pacific sector (Dias and Kiladis 2014; Kiladis et al. 2016).

The MJO envelope is defined here as filtered Tb anomalies of less than -6 K that retain eastward propagating zonal wavenumbers 1–6 and periods between 25 and 96 days (denoted by thick black curves). Instead of presenting space–time filtered field (except for some eastward propagating components as discussed later), as is usually the case in previous studies, we show the phase lines in conjunction with the envelope for a particular Morlet wavelet to demonstrate more clearly how the STWT is effective in elucidating the anatomy of the MJO convection in terms of propagating features. Color dashed lines in the top two panels from

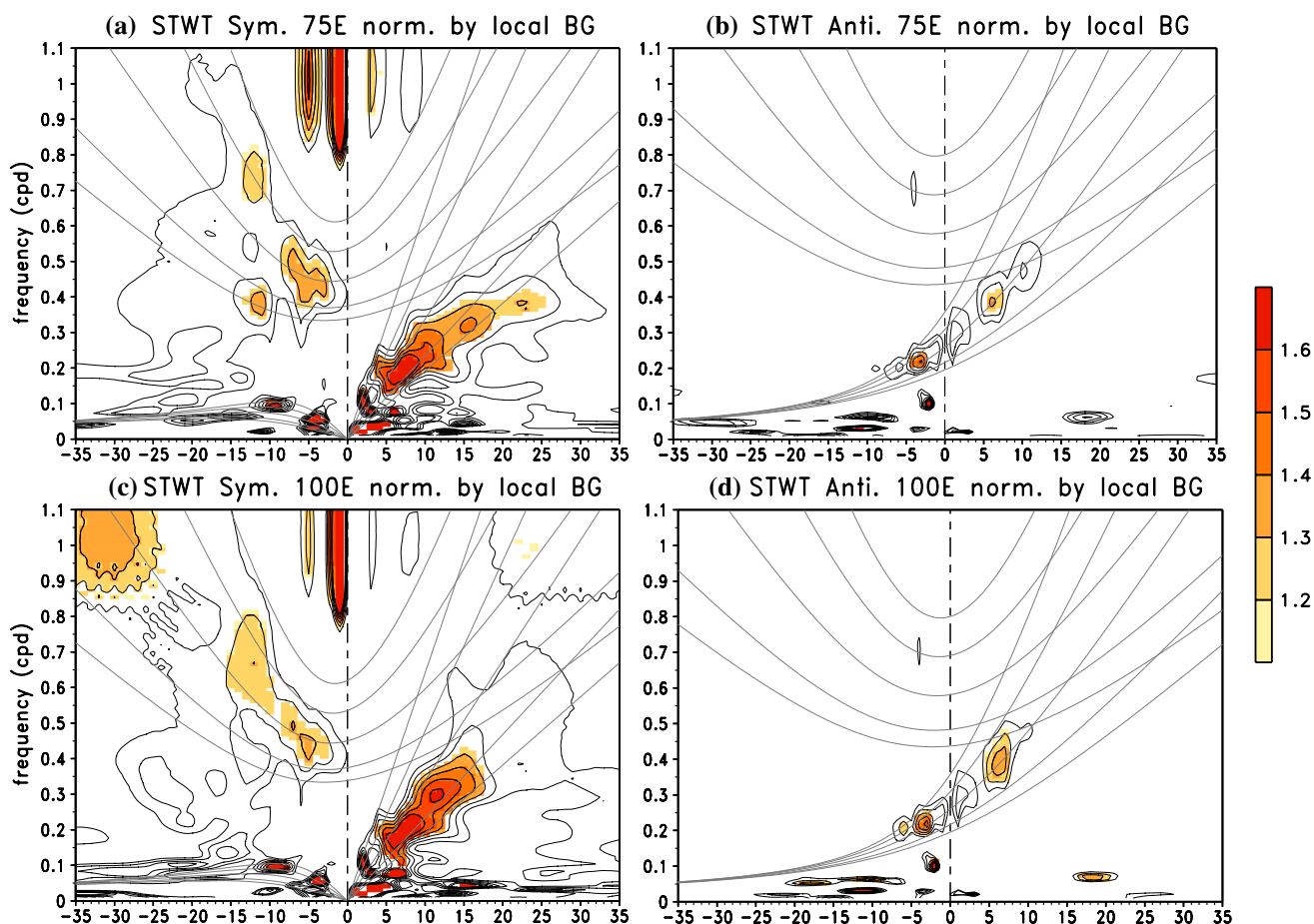


Fig. 5 Same as Fig. 4c, d except for averaged local STWT spectra at (top) 75°E and (bottom) 100°E over the CINDY/DYNAMO period for (left) the symmetric component and (right) the antisymmetric component. The spectra are normalized by their local background spectra, respectively

the left represent the constant phase of the sinusoidal wave embedded within the wave packet (see Fig. 1a) for a particular wavenumber and frequency denoted by corresponding color dots in the STWT spectra (bottom panels). The length of each line represents the e-folding scale in time and space for a particular scale corresponding to the dot of the same color in the spectrum. The white circles in the top panels correspond to the point at which the local STWT spectrum is calculated. The time upon which the spectra are centered was chosen subjectively from the Hovmöller diagrams to correspond to the peak time of the major MJO convective episode at each longitude. In effect, each time appears to correspond to precipitation peaks (as inferred from e.g., TRMM, not shown) associated with certain types of CCEWs, as we now describe.

5.2.1 MJO1

Overall, much of the deep convection on synoptic time scales displays either eastward or westward propagation,

suggesting the predominance of CCEWs. However, close inspection suggests that the space–time scales of these disturbances vary greatly in space and time. Considering MJO1 (Fig. 6), the Hovmöller diagrams show that there was initially active diurnal convective activity to the east of the MJO envelope due to westward propagating convectively coupled gravity waves propagating off of Sumatra around from 16 to 28 October (e.g., Johnson and Ciesielski 2013). The spectral signal of these disturbances appears as a strong peak at 1 cpd centered on westward wavenumber 18 in Fig. 6b (blue dot and phase lines). Later in November these westward waves are no longer significant. Instead, weaker smaller scale quasi-diurnal (blue dot and phase lines in Fig. 6c, d) as well as 2 day disturbances (yellow dot and lines in Fig. 6c, d) become significant, where the latter is reminiscent of the $n=1$ WIG waves also observed during TOGA COARE (e.g., Chen et al. 1996; Takayabu et al. 1996; Haertel and Johnson 1998; Haertel and Kiladis 2004). While diurnal waves show up at both locations, overall the earlier phase of MJO1 (Fig. 6b) is made up of much

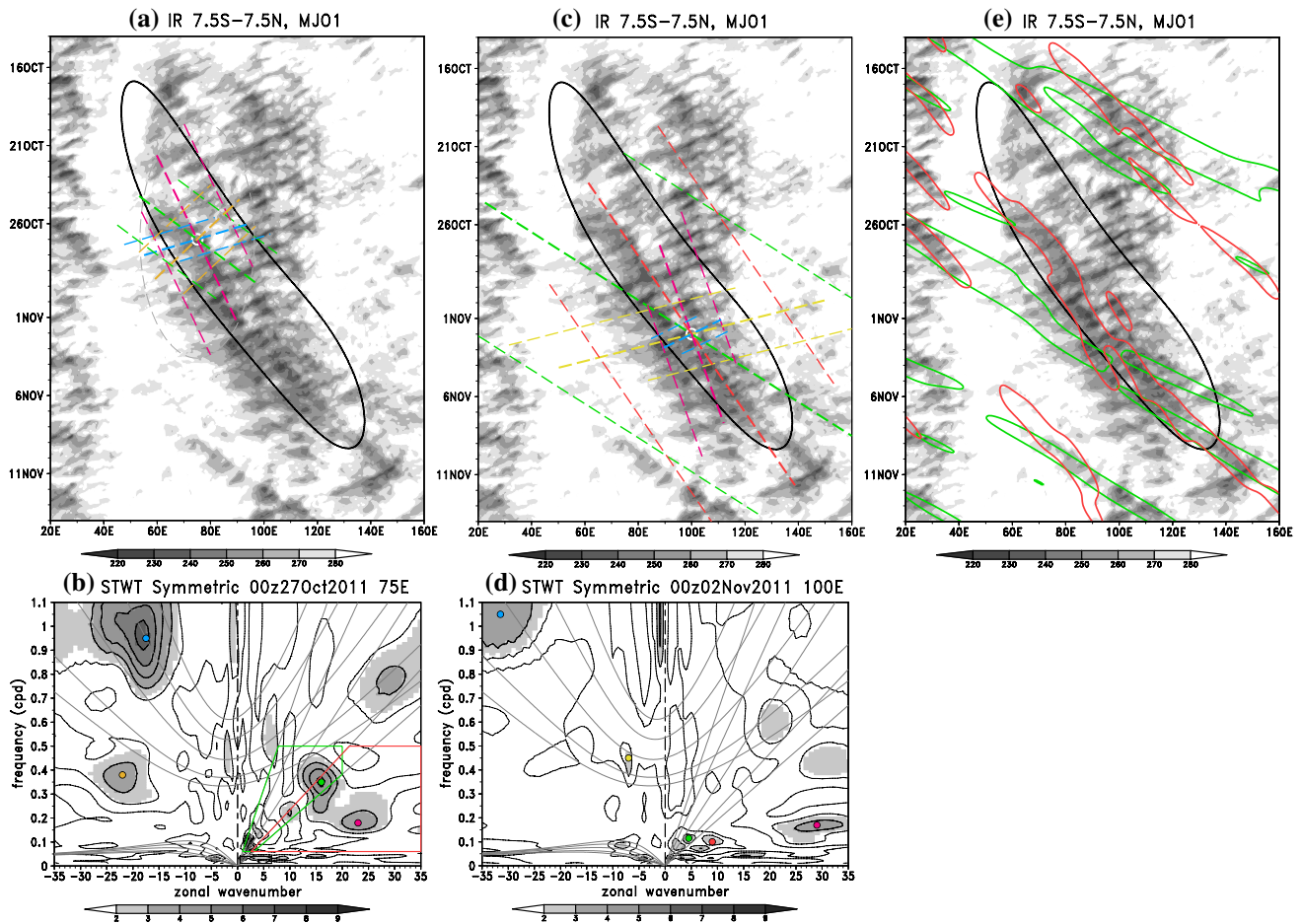


Fig. 6 Hovmöller diagrams of Tb and local STWT spectra for MJO1. *Top* Average Tb over 7.5°S–7.5°N and (*bottom*) the normalized symmetric STWT spectra, for (*left*) 27 October 2011 at 75°E and (*right*) 2 November 2011 at 100°E, by the local background spectrum. *Color dashed lines* in **a** and **c** represent wave troughs of the wave packets for a particular wavenumber and frequency denoted by *color dots* in the bottom panels. The *length of each line* indicates e-folding scale and the e-folding scale is explicitly shown in **a** by a *gray dashed circle* for the slow Kelvin wave component (*magenta*). The *white circles* in **a** and **c** correspond to the point at which the local

STWT spectra are shown. Significance levels at 90, 95, and 99% are 2.3, 3.0, and 4.6, respectively, assuming 2 DOF and shading in the *bottom panels* indicates where the spectral peak is statistically significant at the 90% level. *Heavy solid boxes* in **b** represent regions of wavenumber-frequency filtering for the MJO (*black*), typical Kelvin waves (*green*), and slow Kelvin waves (*red*). *Thick solid black lines* in the top panels represent the MJO-filtered Tb anomalies with contour level of -6 K. *Thick solid green and red lines* in **e** represent the typical and slow Kelvin wave-filtered anomalies, respectively, with contour level of -5 K

more coherent synoptic disturbances than at its latter phase (Fig. 6d) where significant spectral peaks are much weaker.

It is suggested from the Hovmöller diagrams that the commencement of MJO1 is associated with a series of eastward propagating disturbances in middle October, which themselves appear to modulate the westward propagating disturbances within them, reminiscent of Nakazawa's (1988) hypothesis. In this period, the atmosphere became more and more moist (e.g., Johnson and Ciesielski 2013; Powell and Houze 2013; Nasuno et al. 2015; Powell and Houze 2015a), perhaps setting up the stage for the development of the vigorous deep convection that occurred later (i.e., the so-called preconditioning stage, e.g., Kikuchi and Takayabu 2004; Kiladis et al. 2005; Benedict and Randall 2007).

The behavior of CCEWs drastically changes over time within the MJO1 envelope. As in the preconditioning stage, a typical Kelvin wave is seen at both locations that had eastward phase speeds of $10\text{--}12$ m s⁻¹ corresponding to the green phase lines in Fig. 6a,c and dot in Fig. 6b, d, while slower eastward propagating signals were also present as represented by the red and magenta eastward symbols. These slow eastward propagating signals appear to be the major building blocks of the envelope. The wide range in scales of the eastward propagating features represent examples of the “zonally-narrow” components of the MJO as documented by Roundy (2014). Enhancement of planetary-scale, fast Kelvin waves with zonal wavenumber 2 was also seen in the spectra at both locations (Fig. 6b, in particular), which

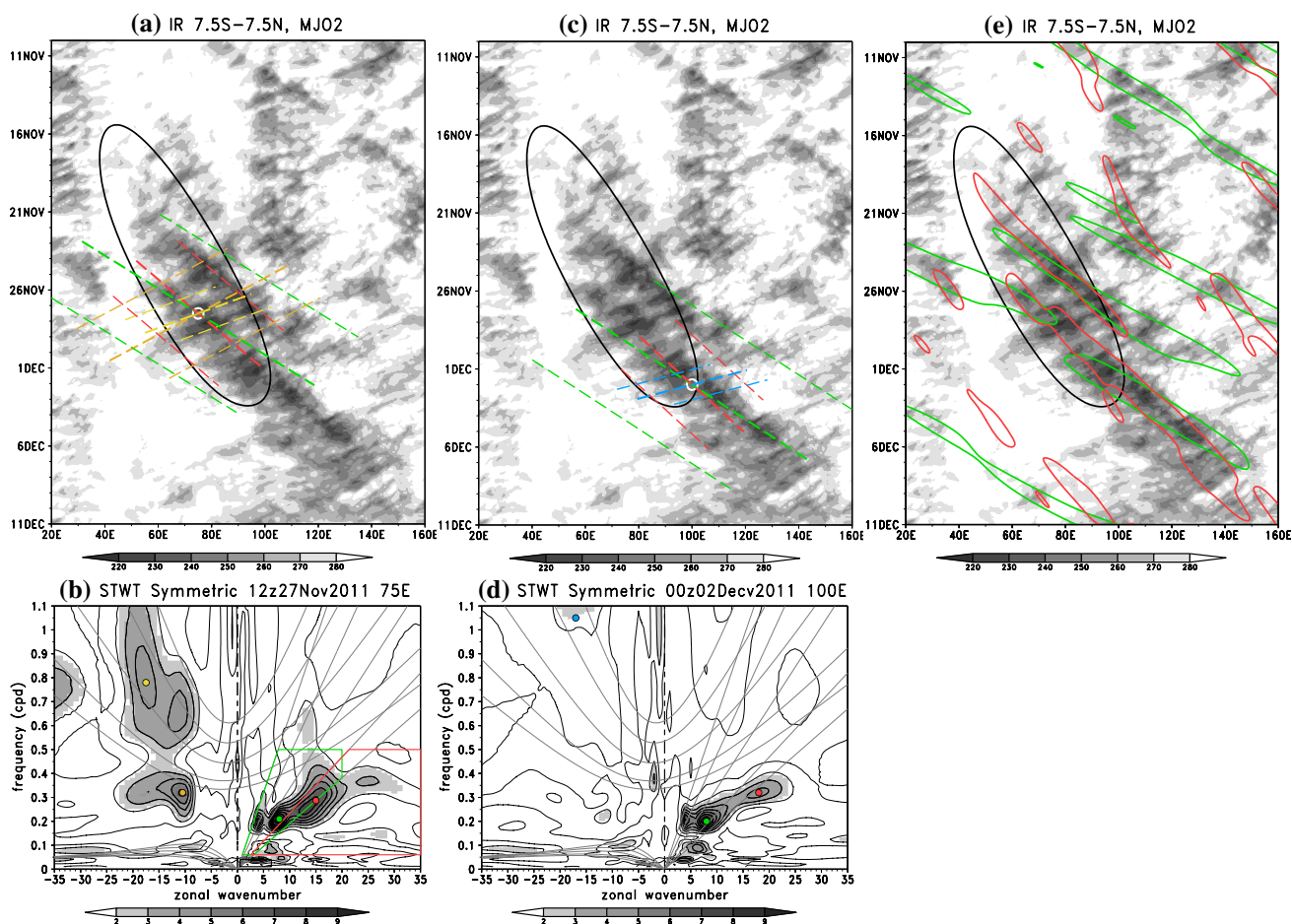


Fig. 7 Same as Fig. 6 except for MJO2

also appears as a distinct spectral peak in the time-averaged spectra (Fig. 5a, c).

The difference in the role of these eastward propagating signals in the MJO convection may become more apparent in terms of space–time filtered anomalies. Based on previous studies and the results in this study, we define two types of filters. One is referred to as a “typical Kelvin wave” filter (denoted by the green box in Fig. 6b) that is similar to but somewhat larger than the one defined in Kiladis et al. (2009) for convectively coupled Kelvin waves. The other filter isolates more slowly eastward propagating signals (denoted by the red box in Fig. 6b), referred to here as the “slow Kelvin wave” filter. The filter design for the slow Kelvin waves is somewhat similar to the zonally narrow MJO band defined by Roundy (2014), although our filter includes much higher wavenumbers and lower frequencies (<0.06 cpd). The filter also includes the region extending to $h_e = 12$ m in order to encompass the spectral peak around $h_e = 8$ m (e.g., Fig. 7b, d), although our results are little affected by the exclusion of this area. Sensitivity tests indicate that exclusion of relatively small wavenumbers up to 10 (i.e., overlapped area

with the zonally narrow MJO band) does not significantly change the results, albeit this yields weaker amplitudes (not shown), suggesting that the term slow Kelvin wave used here is reasonable. It is evident from Fig. 6e that the typical Kelvin wave component, if present, passes through the MJO envelope and does not seem to play a central role in the development of the major convective events within the envelope, whereas the slow Kelvin wave component represents many of the major eastward propagating convective events within the MJO remarkably well.

As in the preconditioning stage, these eastward propagating disturbances appear to conspire with westward propagating waves to cause deep convection to occur, with two different spatio-temporal scales of westward waves (blue dots in Fig. 6b, d) evident at both locations (Kikuchi and Wang 2010). As mentioned above, the diurnal waves at 75°E seem to originate in the Maritime Continent region where the diurnal cycle and its offshore propagation is usually pronounced. It is suggested from the mean spectra (Fig. 5a, c) that these diurnal waves were frequently observed at both locations during CINDY/DYNAMO.

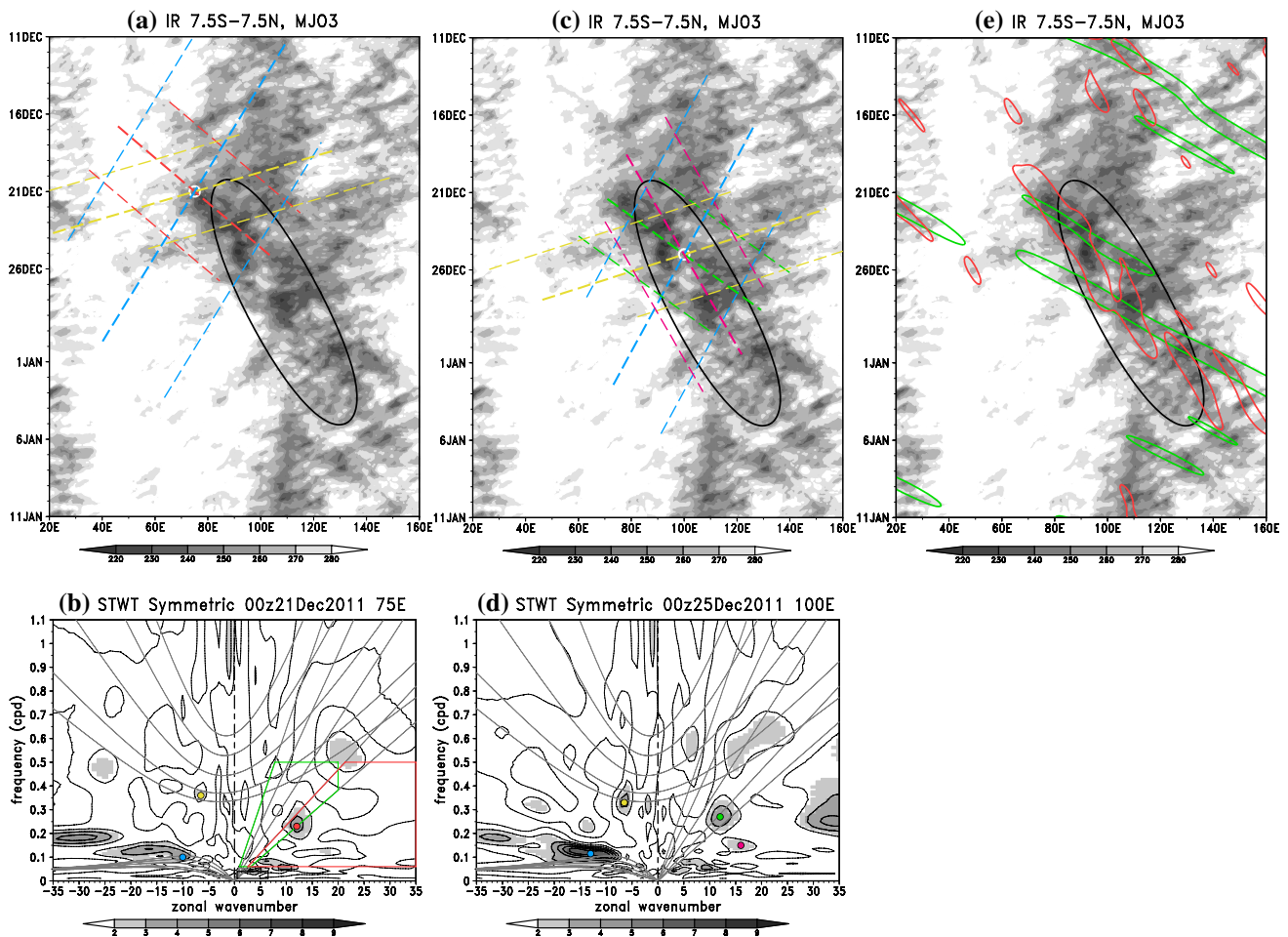


Fig. 8 Same as Fig. 6 except for MJO3

Besides convectively coupled diurnal and $n = 1$ WIG waves, another scale of slower westward propagation is seen centered at wave 22 with a frequency of 0.4 cpd (orange color in Fig. 6a, b), or a bit longer period than 2 days. While this falls within the range of “TD-type” disturbances (e.g., Takayabu and Nitta 1993; Serra et al. 2008) we will show below that the scales of these slower waves vary significantly between MJO events, and are likely not related to true easterly waves, but to off-equatorial “Rossby gyres” as discussed, for example, by Kerns and Chen (2014a, b).

5.2.2 MJO2

In contrast to MJO1, the MJO2 envelope is confined mainly to the IO in terms of MJO-filtered T_b , although a faster convective envelope subsequently extends well into the Pacific during December (Fig. 7), highlighting the nature of the MJO-Kelvin continuum (Roundy 2012, 2014). As in MJO1, there was a preconditioning stage prior to the development

of the major MJO convection starting around November 16 characterized by the passage of westward propagating convective activity embedded within eastward moving envelopes (Fig. 7a, b).

Starting around November 21 the MJO envelope was characterized by two well-defined distinctive Kelvin waves (referred to as “double barrel Kelvin waves” by Gottschalck et al. 2013). The local spectra (Fig. 7b, d) reveal that the Kelvin waves were composed mainly of two distinctive components. A relatively fast component (green) had a phase speed of $\sim 12 \text{ m s}^{-1}$, as is typical of Kelvin waves in this region (e.g., Roundy 2008, 2012, 2014; Kiladis et al. 2009; Yang et al. 2009). In contrast, an even slower component (red) had phase speeds of $\sim 8\text{--}9 \text{ m s}^{-1}$, and this was especially pronounced within the second Kelvin pulse, especially towards the end of the event (Fig. 7c, d). As in MJO1, these Kelvin waves appeared to modulate westward propagating disturbances that include $n = 1$ WIG waves with ~ 1.5 day periodicity at 75°E (yellow), with the diurnal cycle at 100°E , and a slower westward disturbance at 75°E that had closer

to a 3 day period (orange in Fig. 7a, b). Given that the ridge of the slow Kelvin wave spectrum is aligned along $h_e = 8$ m dispersion line, the two filtered Kelvin wave components overlap with each other to some extent (Fig. 7e). In contrast to MJO1, the eastward moving disturbances embedded in MJO during its earlier versus latter stage remain similar.

5.2.3 MJO3

Many aspects of MJO3 are in sharp contrast to MJO1 and MJO2. For example, the MJO filtered convective envelope developed well to the east of both MJO1 and MJO2 and was much shorter in duration. In addition, the earlier stage of MJO3 is made up by much weaker Kelvin waves particularly when compared to the pronounced $n = 1$ ER waves (e.g., Gottschalck et al. 2013), with a relatively small scale of 2000–4000 km (blue in Fig. 8a, b). Another contrast between MJO3 and MJO1/MJO2 is the absence of small scale diurnal and $n = 1$ WIG disturbances.

While signals are weaker in MJO3, convection appeared to be related to a series of Kelvin waves that had a slower phase speed of ~ 9 m s⁻¹ (red in Fig. 8a, b). As these slow Kelvin waves passed through the MJO envelope (green in Fig. 8c, e), even slower eastward propagating signals that moved in line with the envelope (magenta in Fig. 8c, d and red contours in Fig. 8e) developed within the envelope. Throughout MJO3, larger scale $n = 1$ WIG waves relative to MJO1/2 were pronounced (yellow in Fig. 8), which were also examined by Kubota et al. (2015).

5.3 Composite STWT spectra

So far, we have examined the multiscale structure of individual MJO events in a rather subjective manner with particular focus on two locations. In this subsection we take a more objective approach in an attempt to draw more robust conclusions concerning the makeup of the MJO during CINDY/DYNAMO. As in defining the MJO envelope, the MJO convective centers are objectively defined based on the MJO-filtered Tb anomalies as follows: the 7.5°S–7.5°N averaged Tb anomalies are minima in longitude and have less than -8 K. The MJO center locations for MJO1, MJO2, and MJO3 are indicated by the red curves in Fig. 2.

The STWT spectra are composited with respect to the three MJO centers. That is, at each time we check to see if there is an MJO center. If there is, we collect the local symmetric STWT spectrum at the MJO center longitude and the collected spectra are eventually averaged to obtain the composite spectrum. As in the previous subsection, the STWT spectra are normalized by their local background spectra at each longitude prior to making the composite. We assume that EDOF follows (Eq. 11), where n_t is the total number of times used to construct the composite (i.e., ignoring the

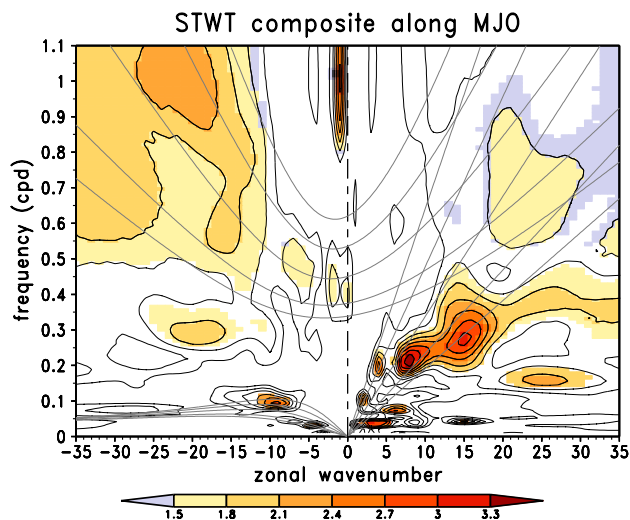


Fig. 9 Composite symmetric STWT spectrum along the MJO phase lines in Fig. 2. Prior to making the composite, the STWT spectra are normalized by their local background spectra. Shading indicates that the spectrum is statistically significant at the 90% level

independence between individual MJO events), which would provide a more conservative estimate.

The composite STWT spectrum is shown in Fig. 9. An enhanced signal of slow Kelvin waves is evident. Besides the MJO peak, there exist four distinctive eastward wave peaks with different equivalent depths: two around 50 m (22 m s⁻¹), one at 15 m (12 m s⁻¹), and just below 8 m (9 m s⁻¹). It is of interest to note the appearance of another significant peak that corresponds to very slow eastward propagation with $k \sim 20$ – 30 and $f \sim 0.16$ cpd (corresponding to ~ 3 m s⁻¹ phase speed). This signal was most apparent in MJO1 at 75°E (Fig. 6b, d) and was also seen in MJO2 at 75°E (Fig. 7b). Whether these waves can be understood in the framework of Kelvin wave dynamics or not is an open question (Roundy 2012, 2014). The separation of scales in the spectral peaks illustrate the broad diversity seen within MJO events during the CINDY/DYNAMO period.

Significant westward propagating signals are also identified. As in the case studies in the previous subsection, westward convectively coupled waves appear to have a wide range of space–time scales that include the strong planetary-scale diurnal peak, the roughly 3-day peak centered on wave -20 , relatively small scale $n = 1$ ER waves, and overall enhancement of power within the $n = 1$ WIG range that includes a pronounced diurnal peak at wave -20 and quasi 2-day peaks over a range of spatial scales. Again, these spectral peaks are dominant at different times, as shown in the case studies in the previous subsection.

One may also be interested in the shape of the spectra during the convective inactive phase of the MJO. Since the convective active area of the MJO covers only a small

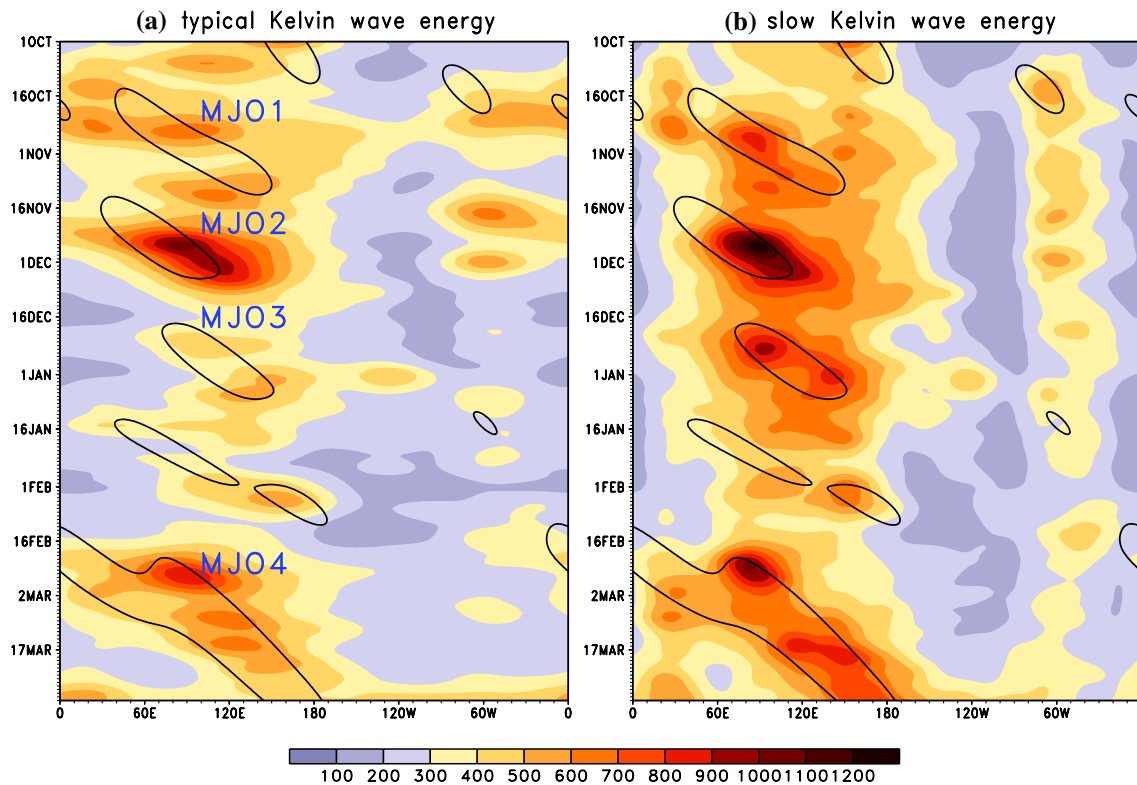


Fig. 10 As in Fig. 2 except for Kelvin wave energy. The Kelvin wave energy is defined at each grid point as integrated symmetric STWT spectra in K^2 over **a** the green box and **b** the red box in Fig. 6b, respectively. Only -4 K contour level is shown for the MJO-filtered Tb anomalies

fraction of the Hovmöller diagram shown in Fig. 2 (e.g., in the IO the area within the MJO for a threshold of -4 K occupies less than 28% for the entire period), a spectral composite for the convective inactive phase of the MJO in the IO resembles, to a large degree, the time-averaged spectra shown in Fig. 5a, c (not shown).

5.4 Relationship between the MJO and Kelvin waves: STWT energy

Finally, we examine how the MJO and the two types of Kelvin wave components (i.e., “typical” and “slow”) are related in terms of wave energy. As discussed above, the STWT provides local spectra at each location and time and their integral over space and time as well as over all space–time scales corresponds to the total energy of the signal (Eq. 3). Thus, the integral of STWT spectrum at a particular location and time over the space–time scales of the wave component in question can be considered to represent the local wave energy of the component (i.e., wave envelope). This can be considered analogous to the variance of space–time Fourier-filtered wave energy for various equatorial waves examined in Dias et al. (2017).

We use the space–time filter boxes shown in Fig. 6b to define the space–time scales of the typical and slow Kelvin

wave components. Figure 10 shows Hovmöller diagrams of the integrated symmetric STWT spectra for both wave components in conjunction with MJO convective envelopes. Both components show a clear contrast between the eastern and western hemispheres, and it is evident that they are strongly associated with the MJO activity, with both components enhanced within and around the MJO envelopes. A closer inspection, however, suggests that the slow Kelvin wave component is more synchronized with the MJO envelopes than the typical Kelvin wave component. Distinctions in the degree of this correspondence can be clearly seen in MJO1 and MJO3.

The above discussion may be well summarized by the pattern correlation in the Hovmöller diagrams between the Kelvin wave energy and the MJO Tb anomalies. The correlations are higher for the slow Kelvin wave component in any particular region (Table 2). As expected, it is particularly high in the warm pool region (nearly -0.6). It is not our intention here to rigorously assess the statistical significance of the correlations, although a rough discussion to gain insight into how these values are likely to be statistically significant is as follows. Based on the MJO space–time scales, a conservative estimate is to suppose that the effective sample size in the longitudinal direction is 4 (i.e., zonal wavenumbers) and in the time direction is 4 (i.e., 45 day

Table 2 Correlation between the MJO and Kelvin wave activity

Area	Global	60°E–180°	60°–120°E
Ordinary Kelvin waves	−0.35	−0.38	−0.42
Slow Kelvin waves	−0.47	−0.59	−0.57

Pattern correlation is computed between the MJO-filtered Tb anomalies and Kelvin wave energy in terms of integrated symmetric STWT spectral energy for typical Kelvin waves and slow Kelvin waves as defined by the green and red boxes in Fig. 6b. In calculating the correlations, the anomalies of Kelvin wave energy is defined as deviations from the time-mean (CINDY/DYNAMO period) energy at each longitude

periodicity). If the data approximately follow Gaussian distributions, significance levels of correlation can be estimated through the so-called Fisher Z transformation (Wilks 2006). This approach yields significant correlations with a sample size of 16 as ± 0.42 and ± 0.48 at the 90 and 95% levels, respectively. These results are relatively insensitive to the choice of the latitudinal band used to define the MJO anomalies (not shown). In contrast, the overlapping area between the typical and slow Kelvin wave components (see Fig. 6b) play different roles in their correlations. The correlations are little affected by the exclusion of the overlapping area for the slow Kelvin wave component, while they become smaller by as much as 0.06 for the typical Kelvin wave counterpart.

One caveat to the above discussion concerns the impact of potentially unrelated background variability on the results of any space–time decomposition method utilized to isolate specific equatorial waves (see discussions in Dias et al. 2012, 2017). We plan to address this issue in more detail within our ongoing study that utilizes the STWT on a long period of Tb data, as discussed below.

6 Summary and discussion

We investigated the relationship between the MJO and CCEWs during the CINDY/DYNAMO field campaign taking advantage of the STWT, which is able to isolate localized space–time spectra at any given location and time. To facilitate use of the STWT, we elaborated upon some practical aspects such as spectral representation and sensitivity to STWT resolution, and also discussed our method of significance testing. The global time-averaged STWT spectral estimates over the CINDY/DYNAMO period yield consistent results with the conventional FT counterparts, with much smoother features in the STWT spectra, suggesting that a local STWT spectral estimate provides a reasonable snapshot. The smoothing nature inherent in the STWT increases the credibility of detecting systematic, significant spectral peaks in an averaged spectrum at the expense of spectral

resolution, a big advantage particularly when dealing with short-term data as in this study.

The averaged CINDY/DYNAMO spectra show an overall good correspondence with long-term averaged (i.e., climatological) spectra, implying that the occurrence of CCEWs during CINDY/DYNAMO were not unusual. The manner in which CCEWs were distributed within the MJO was examined by exploiting the STWT for three MJO events with a particular focus on the IO region. It is, in general, difficult to find universal relationships between the MJO and CCEWs in zonal-wavenumber spectral space, indicative of a broad range in “MJO diversity”, which is in agreement with the conclusion of the statistical studies of Dias et al. (2013, 2017) based on a windowed FT and other approaches.

However, upon close inspection, it is found in all MJO events that a variety of eastward propagating waves appeared to be the major building blocks of the main body of the MJO convection. It is suggested that each CINDY/DYNAMO MJO event was initially associated with Kelvin waves that had space–time scales typical for the IO with a phase speed of $\sim 12 \text{ m s}^{-1}$. Some of the Kelvin waves observed in the latter stages of the MJO, however, tend to have slower phase speeds of $\sim 8\text{--}9 \text{ m s}^{-1}$. This progression was also seen in MJO4 during February–March 2012 (not shown). Sometimes even more slowly eastward propagating disturbances ($3\text{--}5 \text{ m s}^{-1}$) were locally observed. These eastward propagating signals appeared to be associated closely with the most vigorous convection that made up the MJO.

The above-mentioned case study results are well supported by the composite result and wave energy considerations. From the STWT spectral composite (Fig. 9), several Kelvin wave peaks are identified, corresponding to fast ($\sim 23 \text{ m s}^{-1}$), moderate ($\sim 12 \text{ m s}^{-1}$), and slow ($\sim 8 \text{ m s}^{-1}$) phase speeds. The presence of the faster two peaks is expected from the local time-averaged spectra (Fig. 5a, c), although the slow Kelvin wave peak does not appear in the local time-averaged spectra. Also, the signal of even slower disturbances shows up in the composite spectrum, despite not appearing in the local time-averaged spectra. This suggests that these slow eastward propagating waves exist primarily within the MJO, a conclusion that is also supported by the energy considerations made in Sect. 5.4 as well as the studies by Roundy (2008, 2012, 2014). At this stage, it is not clear whether all these disturbances can be classified as Kelvin waves or not. Moreover, it is worthwhile noting that similar slow eastward propagating waves (8 m s^{-1}) were reported to be observed within the MJO during other field campaigns in the IO (Katsumata et al. 2009).

These eastward propagating disturbances alone, however, do not seem to be fully responsible for the development of the major convective systems of the MJO. They often interact with westward propagating disturbances, most of which

can be classified as a wide space–time scale range of $n = 1$ WIG waves, reminiscent of the schematic summary of Nakazawa (1988) that described the hierarchical structure of the MJO: a number of eastward propagating super cloud clusters (“typical” and “slow” Kelvin waves) embedded in the MJO envelope, each being composed of westward propagating cloud clusters. The STWT signals isolated here for the CINDY/DYNAMO period were also shown to be valid for the cases studied by Nakazawa (Kikuchi and Wang 2010). In addition to $n = 1$ WIG waves, other westward disturbances appear at times, although these are not necessarily classifiable as CCEWs.

So far, we have documented a limited number of MJO cases using the STWT approach, however preliminary results from a larger sample indicates that eastward propagating signals are the norm with the MJO convective envelope. Yet, individual MJOs differ widely from each other as well (Dias et al. 2013, 2017). This raises many opportunities for future studies. First, under what conditions do Kelvin waves develop and subsequently slow down within the MJO? The background basic state in which Kelvin waves are embedded varies with the MJO and, as a result, affects the properties of the Kelvin waves through dynamical (e.g., Han and Khouider 2010; Dias and Kiladis 2014) and thermodynamical (e.g., Dias and Pauluis 2011) effects. Of them, the effect of moisture probably plays a central role. The slow Kelvin waves tend to appear at the peak of the MJO convection at which time the entire troposphere tends to be humid (e.g., Johnson and Ciesielski 2013; Nasuno et al. 2015; Yokoi and Sobel 2015; Hannah et al. 2016), which is consistent with the view that convectively coupled waves move slowly under moist conditions because convection effectively reduces the effective static stability (Emanuel et al. 1994).

Our findings are consistent with recent statistical analysis of observational data. Roundy (2012) showed that Kelvin waves tend to have structures more similar to those of the MJO as phase speed decreases with little dependence on the zonal scale. Yasunaga and Mapes (2012) showed that slower Kelvin waves tend to involve more stratiform rain than faster Kelvin waves. Given the similarity in the dynamical fields between the slow Kelvin waves and the MJO, perhaps the emergence of slow Kelvin waves puts an end to the convective active phase of the MJO due to the drying by bringing relatively dry subtropical air into the tropics associated with large-scale Rossby gyres behind the MJO (e.g., Maloney and Hartmann 1998; Kiladis et al. 2005; Benedict and Randall 2007; Yamada et al. 2010; Kerns and Chen 2014a, b).

Another issue has to do with characterizing MJO diversity from the viewpoint of multiscale interaction. In some cases, a wide range of $n = 1$ WIG waves as well as Kelvin waves appear to be the major building blocks of the MJO, but in other cases a wide array of other convectively coupled

waves are seen to be involved. In addition to these rather frequent players, other types of convective organization may come into play from time to time. For example, Judt and Chen (2014) documented the development of explosive MCSs within MJO2 envelope that occurred in association with MRG-like circulations. As seen in Fig. 8, the initiation of MJO3 appeared to be greatly influenced by the moist phase of ER waves. It turns out that while the variance of CCEWs and MCSs is enhanced within the MJO, the ratios between the activity of these various disturbances do not vary much, on average, between active and inactive MJOs, even though individual MJOs can vary greatly from one to another (Dias et al. 2017).

Of course, other, more stationary factors are responsible for the diversity of the MJO as well as of its multiscale structure, such as the seasonal and geographical settings. It has been shown that the behavior of both CCEWs (e.g., Roundy and Frank 2004; Masunaga 2007; Dias and Kiladis 2014; Kikuchi 2014) and the MJO (e.g., Zhang 2005; Kikuchi et al. 2012; Kiladis et al. 2014) are strongly affected by those factors. It is readily expected from the pronounced annual cycle in the MJO that the multiscale structure of the MJO during boreal summer, which displays a strong asymmetric structure about the equator, is different from what we saw in this study. Also, it is likely that the geographical settings affect the multiscale structure, and thus the multiscale interaction of the MJO. Of the different regions, the Maritime Continent perhaps provides the most complex situation in which each wave component undergoes a complicated interaction with the mountainous terrain (Hsu and Lee 2005; Wu and Hsu 2009; Ridout and Flatau 2011) and the pronounced diurnal cycle comes more into play (e.g., Ichikawa and Yasunari 2007, 2008; Fujita et al. 2011; Rauniyar and Walsh 2011; Oh et al. 2012; Peatman et al. 2014). The near-future international field campaign effort, Year of the Maritime Continent (YMC), will provide an unprecedented opportunity to investigate these complex interactions in greater detail.

This is a pilot study that demonstrates the ability of the STWT to elucidate the localized multiscale structure of the MJO during CINDY/DYNAMO. Applying the same type of approach, we are conducting a more robust statistical analysis based on long-term data intending to address some of the aforementioned issues. One goal of this work will be to determine whether MJOs can be grouped by the types of disturbances that reside within them. Results obtained from this morphological-based approach would provide fundamental implications about the interaction between the MJO and CCEWs, which is a basis for further process-oriented analysis in terms of heat, momentum, and moisture (e.g., Kiranmayi and Maloney 2011; Majda and Stechmann 2012; Miyakawa et al. 2012; Zhao et al. 2013; Nasuno et al. 2015).

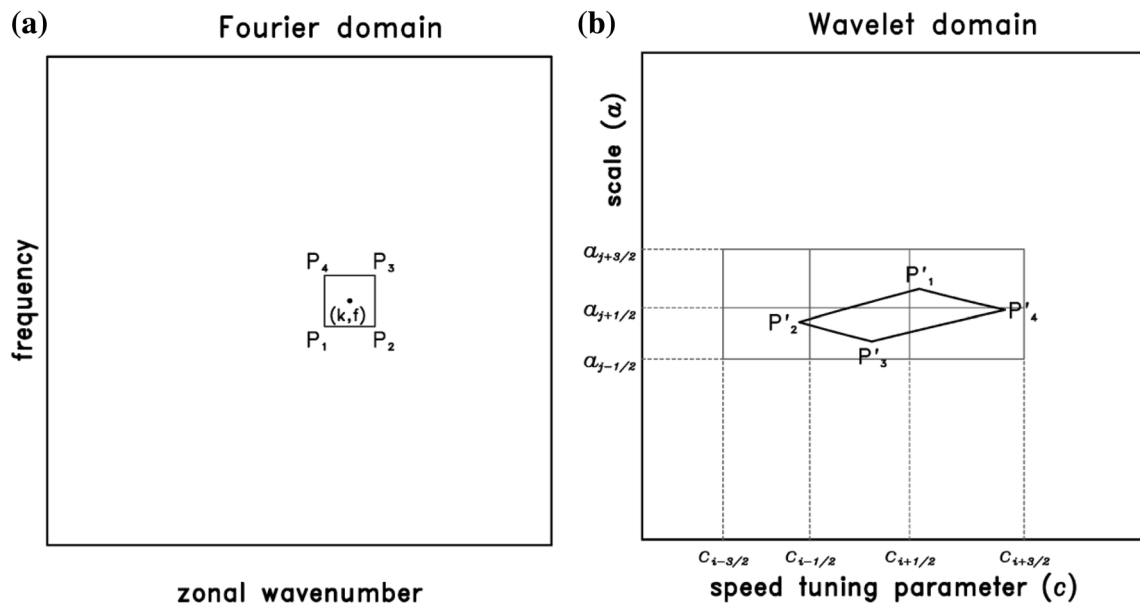


Fig. 11 Schematic illustrating how the STWT spectra are represented in terms of the Fourier space. **a** Spectrum at zonal wavenumber k and frequency f represents the energy contained in a rectangular defined by

$P_1(k - \Delta k/2, f - \Delta f/2)$, $P_2(k + \Delta k/2, f - \Delta f/2)$, $P_3(k + \Delta k/2, f + \Delta f/2)$, $P_4(k - \Delta k/2, f + \Delta f/2)$ and **b** the corresponding energy represented in the wavelet domain. The curves P'_1, P'_2, P'_3, P'_4 , are obtained by means of Eq. (13)

Acknowledgements This research was supported by NOAA Grant NA13OAR4310165. Additional support was provided by the JAMSTEC through its sponsorship of research activities at the IPRC (JIIJ). These results were obtained using the globally-merged full resolution Tb brightness temperature data provided by the climate prediction center/NCEP/NWS (available at http://disc.sci.gsfc.nasa.gov/precipitation/data-holdings/Globally_merged_IR.shtml). The authors acknowledge the use of a package provided by CCSM AMWG to compute Fourier-based zonal wavenumber-frequency power spectrum. We thank three reviewers for their insightful comments. We also benefited from discussion with Paul E. Roundy and Masaki Katsumata. School of Ocean and Earth Science and Technology contribution number 10222 and International Pacific Research Center contribution number 1288.

Appendix: Energy conversion from STWT space to Fourier space

Presenting the calculated STWT spectra in its native space (as a function of scale and speed tuning parameter) makes the STWT difficult to compare with popular FT approaches and hinders interpretation. In order to fill the gap in representation, we developed a method to convert the STWT spectra in terms of zonal wavenumber and frequency. By considering how a sinusoidal wave can be represented in the STWT and FT, a and c can be associated with k and ω as follows (Kikuchi and Wang 2010):

$$\begin{aligned}
 a &= \frac{1}{2} \left(\frac{k_M \omega_M}{k \omega} \right)^{1/2} \\
 c &= \frac{k_M \omega}{k \omega_M}
 \end{aligned}
 \tag{13}$$

where $k_M = k_0 + (k_0^2 + 2)^{1/2}$, $\omega_M = \omega_0 + (\omega_0^2 + 2)^{1/2}$.

In light of the energy conservation (3), the discretized STWT spectrum $\tilde{W}_{i,n}$ in Fourier space at zonal wavenumber k_i and frequency f_n can be estimated using the computed STWT spectrum $W_{j,q}$ at a_j and c_q as

$$|\tilde{W}_{i,n}| = \frac{1}{C_{\psi_{c \neq 0}}} \sum_{j=1}^J \sum_{q=1}^Q \frac{(\log 2)^2}{a_j^2} |W_{j,q}|^2 \frac{\alpha_{i,n;j,q}}{\Delta k \Delta \omega}
 \tag{14}$$

where $\alpha_{i,n;j,q}$ is the coefficient that measures the ratio of the area of the segment (j, q) enclosed by the curves P'_1, P'_2, P'_3, P'_4 to the total area of the segment (j, q) (Fig. 11), and Δk and Δf are the desired zonal wavenumber and frequency resolutions of the $\tilde{W}_{i,n}$ spectrum in the Fourier space.

References

Addison PS (2002) The illustrated wavelet transform handbook: introductory theory and applications in science, engineering, medicine and finance. 1st edn. Taylor & Francis, p 368

- Antoine JP, Murenzi R, Vandergheynst P, Ali ST (2004) Two-dimensional wavelets and their relatives. Cambridge University Press, p 458
- Benedict JJ, Randall DA (2007) Observed characteristics of the MJO relative to maximum rainfall. *J Atmos Sci* 64:2332–2354. doi:10.1175/jas3968.1
- Chen SS, Houze RA Jr, Mapes BE (1996) Multiscale variability of deep convection in relation to large-scale circulation in TOGA COARE. *J Atmos Sci* 53:1380–1409
- Dias J, Kiladis GN (2014) Influence of the basic state zonal flow on convectively coupled equatorial waves. *Geophys Res Lett* 41:6904–6913. doi:10.1002/2014gl061476
- Dias J, Pauluis O (2011) Modulations of the phase speed of convectively coupled Kelvin waves by the ITCZ. *J Atmos Sci* 68:1446–1459. doi:10.1175/2011jas3630.1
- Dias J, Tulich SN, Kiladis GN (2012) An object-based approach to assessing the organization of tropical convection. *J Atmos Sci* 69:2488–2504. doi:10.1175/jas-d-11-0293.1
- Dias J, Leroux S, Tulich SN, Kiladis GN (2013) How systematic is organized tropical convection within the MJO? *Geophys Res Lett* 40:1420–1425. doi:10.1002/grl.50308
- Dias J, Sakaeda N, Kiladis GN, Kikuchi K (2017) Influences of the MJO on space-time tropical convection organization. *J Geophys Res Atmos*. doi:10.1002/2017JD026526
- Dunkerton TJ, Crum FX (1995) Eastward propagating similar to 2- to 15-day equatorial convection and its relation to the tropical intraseasonal oscillation. *J Geophys Res Atmos* 100:25781–25790
- Emanuel KA, Neelin JD, Bretherton CS (1994) On large-scale circulations in convecting atmospheres. *Q J R Meteorol Soc* 120:1111–1143
- Fujita M, Yoneyama K, Mori S, Nasuno T, Satoh M (2011) Diurnal convection peaks over the eastern Indian Ocean off Sumatra during different MJO phases. *J Meteorol Soc Jpn* 89A:317–330. doi:10.2151/jmsj.2011-A22
- Gottschalck J, Roundy PE, Schreck CJ, Vintzileos A, Zhang C (2013) Large-scale atmospheric and oceanic conditions during the 2011–2012 DYNAMO field campaign. *Mon Weather Rev* 141:4173–4196. doi:10.1175/mwr-d-13-00022.1
- Haertel PT, Johnson RH (1998) Two-day disturbances in the equatorial western Pacific. *Q J R Meteorol Soc* 124:615–636
- Haertel PT, Kiladis GN (2004) Dynamics of 2-day equatorial waves. *J Atmos Sci* 61:2707–2721
- Han Y, Khouider B (2010) Convectively coupled waves in a sheared environment. *J Atmos Sci* 67:2913–2942
- Hannah WM, Mapes BE, Elsaesser GS (2016) A Lagrangian view of moisture dynamics during DYNAMO. *J Atmos Sci* 73:1967–1985. doi:10.1175/jas-d-15-0243.1
- Hendon HH, Wheeler MC (2008) Some space-time spectral analyses of tropical convection and planetary-scale waves. *J Atmos Sci* 65:2936–2948
- Hodges KI, Chappell DW, Robinson GJ, Yang G (2000) An improved algorithm for generating global window brightness temperatures from multiple satellite infrared imagery. *J Atmos Ocean Technol* 17:1296–1312
- Hsu HH, Lee MY (2005) Topographic effects on the eastward propagation and initiation of the Madden–Julian oscillation. *J Clim* 18:795–809
- Hung MP, Lin JL, Wang WQ, Kim D, Shinoda T, Weaver SJ (2013) MJO and convectively coupled equatorial waves simulated by CMIP5 climate models. *J Clim* 26:6185–6214. doi:10.1175/jcli-d-12-00541.1
- Ichikawa H, Yasunari T (2007) Propagating diurnal disturbances embedded in the Madden–Julian Oscillation. *Geophys Res Lett*. doi:10.1029/2007gl030480
- Ichikawa H, Yasunari T (2008) Intraseasonal variability in diurnal rainfall over New Guinea and the surrounding oceans during Austral summer. *J Clim* 21:2852–2868
- Janowiak JE, Joyce RJ, Yarosh Y (2001) A real-time global half-hourly pixel-resolution infrared dataset and its applications. *Bull Am Meteorol Soc* 82:205–217
- Johnson RH, Ciesielski PE (2013) Structure and properties of Madden–Julian oscillations deduced from DYNAMO sounding arrays. *J Atmos Sci* 70:3157–3179
- Johnson RH, Ciesielski PE, Ruppert JH Jr, Katsumata M (2015) Sounding-based thermodynamic budgets for DYNAMO. *J Atmos Sci* 72:598–622. doi:10.1175/jas-d-14-0202.1
- Judt F, Chen SS (2014) An explosive convective cloud system and its environmental conditions in MJO initiation observed during DYNAMO. *J Geophys Res Atmos* 119:2781–2795. doi:10.1002/2013jd021048
- Katsumata M, Johnson RH, Ciesielski PE (2009) Observed synoptic-scale variability during the developing phase of an ISO over the Indian Ocean during MISO. *J Atmos Sci* 66:3434–3448. doi:10.1175/2009jas3003.1
- Kerns BW, Chen SS (2014a) Equatorial dry air intrusion and related synoptic variability in MJO Initiation during DYNAMO. *Mon Weather Rev* 142:1326–1343. doi:10.1175/mwr-d-13-00159.1
- Kerns BW, Chen SS (2014b) ECMWF and GFS model forecast verification during DYNAMO: Multiscale variability in MJO initiation over the equatorial Indian Ocean. *J Geophys Res Atmos* 119:3736–3755. doi:10.1002/2013jd020833
- Kikuchi K (2014) An introduction to combined Fourier-wavelet transform and its application to convectively coupled equatorial waves. *Clim Dyn* 43:1339–1356. doi:10.1007/s00382-013-1949-8
- Kikuchi K, Takayabu YN (2004) The development of organized convection associated with the MJO during TOGA COARE IOP: trimodal characteristics. *Geophys Res Lett* 31:L10101. doi:10.1029/2004GL019601
- Kikuchi K, Wang B (2008) Diurnal precipitation regimes in the global tropics. *J Clim* 21:2680–2696. doi:10.1175/2007jcli2051.1
- Kikuchi K, Wang B (2010) Spatiotemporal wavelet transform and the multiscale behavior of the Madden–Julian oscillation. *J Clim* 23:3814–3834
- Kikuchi K, Wang B, Kajikawa Y (2012) Bimodal representation of the tropical intraseasonal oscillation. *Clim Dyn* 38:1989–2000. doi:10.1007/s00382-011-1159-1
- Kikuchi K, Kodama C, Nasuno T, Nakano M, Miura H, Satoh M, Noda A, Yamada Y (2017) Tropical intraseasonal oscillation in an AMIP-type experiment by NICAM. *Clim Dyn*. doi:10.1007/s00382-016-3219-z
- Kiladis GN, Straub KH, Haertel PT (2005) Zonal and vertical structure of the Madden–Julian oscillation. *J Atmos Sci* 62:2790–2809
- Kiladis GN, Wheeler MC, Haertel PT, Straub KH, Roundy PE (2009) Convectively coupled equatorial waves. *Rev Geophys* 47:RG2003. doi:10.1029/2008RG000266
- Kiladis GN, Dias J, Straub KH, Wheeler MC, Tulich SN, Kikuchi K, Weickmann KM, Ventrone MJ (2014) A comparison of OLR and circulation-based indices for tracking the MJO. *Mon Weather Rev* 142:1697–1715. doi:10.1175/mwr-d-13-00301.1
- Kiladis GN, Dias J, Gehne M (2016) The relationship between equatorial mixed Rossby-gravity and eastward inertio-gravity waves. Part I. *J Atmos Sci* 73:2123–2145. doi:10.1175/jas-d-15-0230.1
- Kiranmayi L, Maloney ED (2011) Intraseasonal moist static energy budget in reanalysis data. *J Geophys Res Atmos*. doi:10.1029/2011jd016031
- Kubota H, Yoneyama K, Hamada J-I, Wu P, Sudaryanto A, Wahyono IB (2015) Role of Maritime Continent convection during the preconditioning stage of the Madden–Julian oscillation observed in CINDY2011/DYNAMO. *J Meteorol Soc Jpn* 93A:101–114. doi:10.2151/jmsj.2015-050

- Kumar P, Foufoula-Georgiou E (1997) Wavelet analysis for geophysical applications. *Rev Geophys* 35:385–412
- Lau WKM, Waliser D (eds) (2012) *Intraseasonal variability in the atmosphere–ocean climate system*. 2nd edn. Springer, p 614
- Madden RA, Julian PR (1971) Detection of a 40–50 day oscillation in the zonal wind in the tropical Pacific. *J Atmos Sci* 28:702–708
- Madden RA, Julian PR (1972) Description of global-scale circulation cells in tropics with a 40–50 day period. *J Atmos Sci* 29:1109–1123
- Majda AJ, Stechmann SN (2012) *Multiscale theories for the MJO. Intraseasonal variability in the atmosphere–ocean climate system*, 2nd edn. Lau KM, Waliser DE (eds) Springer, pp 549–585
- Maloney ED, Hartmann DL (1998) Frictional moisture convergence in a composite life cycle of the Madden–Julian oscillation. *J Clim* 11:2387–2403
- Mapes BE, Houze RA Jr (1993) Cloud clusters and superclusters over the oceanic warm pool. *Mon Weather Rev* 121:1398–1415
- Masunaga H (2007) Seasonality and regionality of the Madden–Julian oscillation, Kelvin wave, and equatorial Rossby wave. *J Atmos Sci* 64:4400–4416. doi:10.1175/2007jas2179.1
- Masunaga H, L'Ecuyer TS, Kummerow CD (2006) The Madden–Julian oscillation recorded in early observations from the tropical rainfall measuring mission (TRMM). *J Atmos Sci* 63:2777–2794
- Matsuno T (1966) Quasi-geostrophic motions in the equatorial area. *J Meteorol Soc Jpn* 44:25–43
- Meyers SD, Kelly BG, O'Brien JJ (1993) An introduction to wavelet analysis in oceanography and meteorology: with application to the dispersion of Yanai waves. *Mon Weather Rev* 121:2858–2866
- Miyakawa T, Takayabu YN, Nasuno T, Miura H, Satoh M, Moncrieff MW (2012) Convective momentum transport by rainbands within a Madden–Julian oscillation in a global nonhydrostatic model with explicit deep convective processes. Part I: Methodology and general results. *J Atmos Sci* 69:1317–1338. doi:10.1175/jas-d-11-024.1
- Mori S, Jun-Ichi H, Tauhid YI, Yamanaka MD (2004) Diurnal land–sea rainfall peak migration over Sumatera Island, Indonesian maritime continent, observed by TRMM satellite and intensive rawinsonde soundings. *Mon Weather Rev* 132:2021–2039
- Nakazawa T (1988) Tropical super clusters within intraseasonal variations over the western Pacific. *J Meteorol Soc Jpn* 66:823–839
- Nasuno T, Li T, Kikuchi K (2015) Moistening processes before the convective initiation of Madden–Julian oscillation events during the CINDY2011/DYNAMO period. *Mon Weather Rev* 143:622–643. doi:10.1175/mwr-d-14-00132.1
- Oh J-H, Kim K-Y, Lim G-H (2012) Impact of MJO on the diurnal cycle of rainfall over the western Maritime Continent in the Austral summer. *Clim Dyn* 38:1167–1180. doi:10.1007/s00382-011-1237-4
- Peatman SC, Matthews AJ, Stevens DP (2014) Propagation of the Madden–Julian oscillation through the Maritime Continent and scale interaction with the diurnal cycle of precipitation. *Q J R Meteorol Soc* 140:814–825. doi:10.1002/qj.2161
- Powell SW, Houze RA Jr (2015a) Effect of dry large-scale vertical motions on initial MJO convective onset. *J Geophys Res Atmos* 120:4783–4805. doi:10.1002/2014jd022961
- Powell SW, Houze RA Jr (2015b) Evolution of precipitation and convective echo top heights observed by TRMM radar over the Indian Ocean during DYNAMO. *J Geophys Res Atmos* 120:3906–3919. doi:10.1002/2014jd022934
- Powell SW, Houze RA, Jr. (2013) The cloud population and onset of the Madden–Julian Oscillation over the Indian Ocean during DYNAMO-AMIE. *J Geophys Res Atmos* 118:11979–11995. doi:10.1002/2013jd020421
- Rauniyar SP, Walsh KJE (2011) Scale interaction of the diurnal cycle of rainfall over the Maritime Continent and Australia: influence of the MJO. *J Clim* 24:325–348. doi:10.1175/2010jcli3673.1
- Ridout JA, Flatau MK (2011) Kelvin wave time scale propagation features of the Madden–Julian Oscillation (MJO) as measured by the Chen–MJO index. *J Geophys Res Atmos*. doi:10.1029/2011jd015925
- Roundy PE (2008) Analysis of convectively coupled Kelvin waves in the Indian ocean MJO. *J Atmos Sci* 65:1342–1359
- Roundy PE (2012) Observed structure of convectively coupled waves as a function of equivalent depth: Kelvin waves and the Madden–Julian Oscillation. *J Atmos Sci* 69:2097–2106. doi:10.1175/jas-d-12-03.1
- Roundy PE (2014) Regression analysis of zonally narrow components of the MJO. *J Atmos Sci* 71:4253–4275. doi:10.1175/jas-d-13-0288.1
- Roundy PE, Frank WM (2004) A climatology of waves in the equatorial region. *J Atmos Sci* 61:2105–2132
- Serra YL, Kiladis GN, Cronin MF (2008) Horizontal and vertical structure of easterly waves in the Pacific ITCZ. *J Atmos Sci* 65:1266–1284
- Sobel A, Wang S, Kim D (2014) Moist static energy budget of the MJO during DYNAMO. *J Atmos Sci* 71:4276–4291. doi:10.1175/jas-d-14-0052.1
- Takayabu YN (1994a) Large-scale cloud disturbances associated with equatorial waves. Part I: Spectral features of the cloud disturbances. *J Meteorol Soc Jpn* 72:433–449
- Takayabu YN (1994b) Large-scale cloud disturbances associated with equatorial waves. Part II: Westward-propagating inertio-gravity waves. *J Meteorol Soc Japan* 72:451–465
- Takayabu YN, Nitta T (1993) 3–5 day-period disturbances coupled with convection over the tropical Pacific Ocean. *J Meteorol Soc Jpn* 71:221–246
- Takayabu YN, Lau KM, Sui CH (1996) Observation of a quasi-2-day wave during TOGA COARE. *Mon Weather Rev* 124:1892–1913
- Torrence C, Compo GP (1998) A practical guide to wavelet analysis. *Bull Am Meteorol Soc* 79:61–78
- Waliser D (2012) *Predictability and forecasting. Intraseasonal variability in the atmosphere–ocean climate system*, 2nd edn. Lau WKM, Waliser DE (eds) Praxis Publishing, pp 433–476
- Wang B (2012) *Theories. Intraseasonal variability in the atmosphere–ocean climate system*, 2nd edn. Lau KM, Waliser DE (eds) Springer, pp 335–398
- Wheeler MC, Hendon HH (2004) An all-season real-time multivariate MJO index: development of an index for monitoring and prediction. *Mon Weather Rev* 132:1917–1932
- Wheeler M, Kiladis GN (1999) Convectively coupled equatorial waves: analysis of clouds and temperature in the wavenumber-frequency domain. *J Atmos Sci* 56:374–399
- Wilks DS (2006) *Statistical methods in the atmospheric sciences*. 2nd edn. Academic Press, p 648
- Wu C-H, Hsu H-H (2009) Topographic influence on the MJO in the maritime continent. *J Clim* 22:5433–5448. doi:10.1175/2009jcli2825.1
- Yamada H, Yoneyama K, Katsumata M, Shirooka R (2010) Observations of a super cloud cluster accompanied by synoptic-scale eastward-propagating precipitating systems over the Indian Ocean. *J Atmos Sci* 67:1456–1473
- Yang GY, Slingo J (2001) The diurnal cycle in the tropics. *Mon Weather Rev* 129:784–801
- Yang G-Y, Slingo J, Hoskins B (2009) Convectively coupled equatorial waves in high-resolution Hadley Centre climate models. *J Clim* 22:1897–1919. doi:10.1175/2008jcli2630.1
- Yasunaga K, Mapes B (2012) Differences between more divergent and more rotational types of convectively coupled equatorial waves. Part II: Composite analysis based on space-time filtering. *J Atmos Sci* 69:17–34
- Yokoi S, Sobel A (2015) Intraseasonal variability and seasonal march of the moist static energy budget over the eastern Maritime

- Continent during CINDY2011/DYNAMO. *J Meteorol Soc Jpn* 93A:81–100. doi:[10.2151/jmsj.2015-041](https://doi.org/10.2151/jmsj.2015-041)
- Yoneyama K, Zhang C, Long CN (2013) Tracking pulses of the Madden–Julian oscillation. *Bull Am Meteorol Soc* 94:1871–1891. doi:[10.1175/bams-d-12-00157.1](https://doi.org/10.1175/bams-d-12-00157.1)
- Zhang CD (2005) Madden–Julian oscillation. *Rev Geophys* 43:RG2003. doi:[10.1029/2004RG000158](https://doi.org/10.1029/2004RG000158)
- Zhang CD (2013) Madden–Julian oscillation: bridging weather and climate. *Bull Am Meteorol Soc* 94:1849–1870. doi:[10.1175/bams-d-12-00026.1](https://doi.org/10.1175/bams-d-12-00026.1)
- Zhao C, Li T, Zhou T (2013) Precursor signals and processes associated with MJO initiation over the tropical Indian Ocean. *J Clim* 26:291–307. doi:[10.1175/jcli-d-12-00113.1](https://doi.org/10.1175/jcli-d-12-00113.1)